TOPICAL REVIEW

Major minority: energetic particles in fusion plasmas

B N Breizman[1] **and S E Sharapov**[2]

[1] Institute for Fusion Studies, The University of Texas at Austin, TX 78712, USA
[2] EURATOM/CCFE Fusion Association, Culham Science Centre, Abingdon OX14 3DB, UK

Abstract
This paper describes advances made in the field of energetic-particle physics
since the topical review of Alfvén eigenmode observations in toroidal plasmas
(Wong 1999 *Plasma Phys. Control. Fusion* **41** R1–R56). The development of
plasma confinement scenarios with reversed magnetic shear and significant
population of energetic particles, and the development of novel energetic-
particle diagnostics were the main milestones in the past decade, and these are
the main experimental subjects of this review. The theory of Alfvén cascade
eigenmodes in reversed-shear tokamaks and its use in magnetohydrodynamic
spectroscopy are presented. Based on experimental observations and nonlinear
theory of energetic-particle instabilities in the near-threshold regime, the
frequency-sweeping events for spontaneously formed phase-space holes and
clumps and the evolution of the fishbone oscillations are described. The multi-
mode scenarios of enhanced particle transport are discussed and a brief summary
is given of several engaging research topics that are beyond the authors' direct
involvement.

(Some figures in this article are in colour only in the electronic version)

1. Introduction

The need to control the behaviour of the energetic ion population and associated instabilities
is one of the key issues for magnetic fusion [1]. Alfvénic instabilities are of primary interest
as well as a primary concern in that regard. They have received an overwhelming amount
of attention after toroidal Alfvén eigenmodes (TAEs) were predicted theoretically [2] and
shown to be susceptible to excitation by fast ions in burning plasmas [3]. An experimental
search for TAEs on TFTR [4] and DIII-D [5] has convincingly confirmed their existence.
Extended subsequent world-wide studies of TAEs, both experimental and theoretical, are
summarized in [6].

In the past decade, the development of new plasma scenarios with internal transport
barriers (ITBs) and reversed magnetic shear has revealed instabilities of Alfvén cascade
(AC) eigenmodes [7–9] with characteristics quite different from TAEs. At the same time,
the spherical tokamak (ST) avenue of magnetic fusion was successfully explored with two
new mega-ampere machines MAST and NSTX achieving very high values of β in the

presence of super-Alfvénic neutral beam injection (NBI) [10, 11]. These MAST and NSTX experiments have shown a variety of NBI-driven frequency-sweeping events in the Alfvénic range, which calls for an adequate theoretical description of the conjectured non-perturbative nonlinear modes.

Significant progress has been made in diagnostics of energetic-particle-driven modes. The development of novel mode detection techniques based on interferometry [12, 13] and phase contrast imaging (PCI) [14], together with improved reflectometry [15, 16], made the characterization of unstable modes and their amplitudes more reliable. With these diagnostics at hand, the theory-to-experiment comparison became less ambiguous for all types of modes, including TAEs. In particular, the interpretation of experiments with multiple modes excited simultaneously, became possible and consistent with the experimental data [17, 18].

Thanks to the close interaction between theory and experiment, the experimentally observed modes driven by energetic particles have become a convenient tool for so-called magnetohydrodynamic (MHD) spectroscopy first discussed in detail in [19] and developed experimentally in [8, 20]. This type of diagnostics delivers unique information about plasma properties and plasma equilibrium from the experimentally measured spectra of discrete Alfvén eigenmodes. In particular, a routine use of the observed ACs in shear-reversed plasmas has helped a great deal in developing ITB scenarios [21].

The advances in the theoretical description of nonlinear mode evolution have been largely due to the exploration of the near-threshold regimes typical for most of the energetic-particle-driven waves [22]. The near-threshold situation develops naturally when the energetic-particle population builds up gradually and the energetic-particle drive becomes competitive with the mode damping. The near-threshold evolution of the mode can be characterized as either soft or hard. In the first case, the mode saturates at a low level reflecting the closeness to the instability threshold. In the case of hard excitation, the nonlinearity acts to destabilize the mode and push the system further away from the threshold. Both soft and hard scenarios have been observed experimentally. The developed theoretical approach has been applied successfully to TAEs [23–25] and fishbones [26] in an effort to characterize nonlinear evolution of isolated weakly unstable modes and to use this understanding to interpret measurements of the modes and fast ions.

A more challenging physics problem to address is multi-mode transport of energetic particles. This essential step is required to predict with confidence the macroscopic effects of the modes on energetic particles in burning plasma machines such as ITER [1]. In contrast to present-day experiments with typical ratio between the orbit width and the minor radius of plasma $\rho_\alpha/a \cong 0.1$, ITER will have much larger dimensions and $\rho_\alpha/a \cong 10^{-3}$–$10^{-2}$. Under such conditions, a single mode cannot affect the transport on a global scale, and only multiple modes can if they provide overlap of the wave–particle resonances over a significant part of the minor radius.

The aim of this paper is to review the ongoing theoretical and experimental studies of energetic-particle-driven instabilities and their nonlinear consequences. The content of the review is largely influenced by our personal research preferences, which obviously makes the paper less than comprehensive. Yet, we hope that this deliberately biased description does not overlook the most challenging points in the continuing effort to complete the energetic-particle puzzle. The rest of the paper is organized as follows. Section 2 describes ACs in tokamak plasmas with reversed magnetic shear and their use in MHD spectroscopy. Section 3 deals with nonlinear properties of the modes driven by energetic particles. Section 4 presents our current understanding of the bursty 'fishbone' instability. Global transport of energetic particles due to multiple unstable modes is described in section 5. The concluding section (section 6) is an outline of broader research activities.
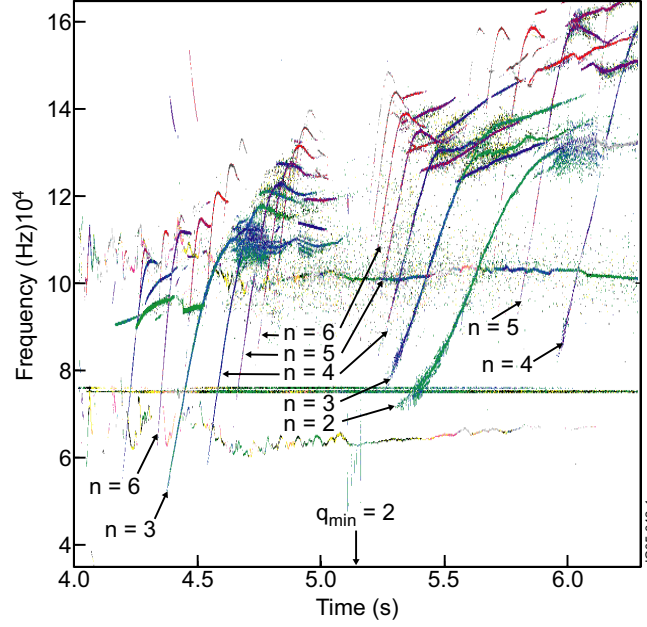
Figure 1. Magnetic spectrogram (Fourier decomposition of the Mirnov coil signal) showing an example of ICRH-driven ACs with different toroidal mode numbers in a JET reversed-shear plasma. Reprinted with permission from [9]. Copyright 2011, American Institute of Physics.

2. Alfvén modes in plasmas with reversed magnetic shear

2.1. AC eigenmodes

In the past decade, significant attention was paid to advanced tokamak scenarios aimed at obtaining ITBs with non-monotonic safety factor profiles $q(r)$. Such plasmas have a region of magnetic shear reversal, which enriches their Alfvén wave spectra. In addition to the arising multiplicity [27] of TAEs [2] in the low-shear limit, these plasmas commonly exhibit the so-called ACs [7–9, 21], also known as reversed-shear Alfvén eigenmodes (RSAEs) [16]. ACs have been observed on JET [7–9, 21], JT-60U [28, 29], C-MOD [14], TFTR [30] and DIII-D [13]. They are excited by either ICRH-accelerated ions (JET, JT-60U and C-MOD) or by NBI-produced ions (JET, JT-60U, and DIII-D). Fusion born alpha particles excited the ACs in TFTR DT plasmas [30], indicating the relevance of these modes to burning plasma experiments.

   The AC modes, an example of which is shown in figure 1, are associated with the extremum point of the shear Alfvén continuum localized at the magnetic surface with the minimum value of $q(r)$, labelled as q_0 [7–9, 21].

   During time evolution of the plasma current, the eigenfrequency of the AC, $\omega_{AC}(t)$, changes in step with $q_0(t)$ in accordance with the local dispersion relation for shear Alfvén waves. In the simplest case of cold (low pressure) plasma, this gives

$$\omega_{AC}(t) \approx \frac{V_A}{R_0} \left| n - \frac{m}{q_0(t)} \right| + \Delta\omega. \tag{2.1}$$

Here, n and m are toroidal and poloidal mode numbers, R_0 is the major radius of the tokamak, $V_A = B_0/(4\pi\rho_0)^{1/2}$ is the Alfvén speed, B_0 is the equilibrium magnetic field and ρ_0 is the mass density of the plasma. The first (dominant) term on the right-hand side of (2.1) is the shear Alfvén continuum frequency at the zero shear point.
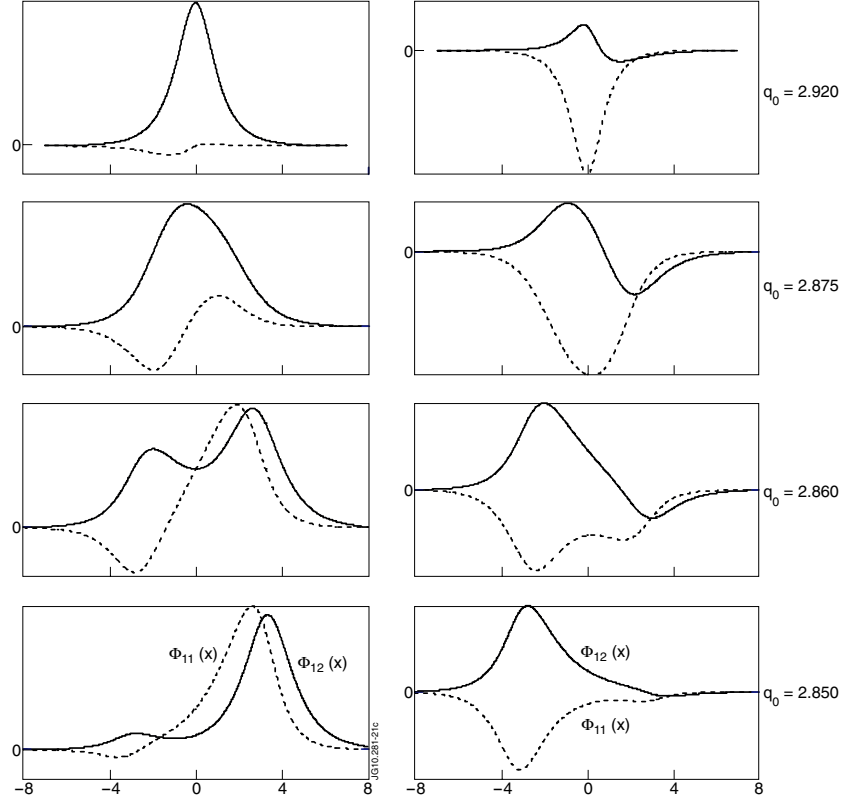
3

Figure 2. Snapshots of the mode structure for $n = 4$ and $m = (12; 11)$ during the transition from AC to TAE. The left column shows the radial profiles of the poloidal components for the even parity TAE; the right column presents the odd parity mode [32]. Reprinted with permission from [32]. Copyright 2011, American Institute of Physics.

The correction $\Delta\omega$ in (2.1) describes a deviation of the AC eigenfrequency from the continuum, and it originates from the effects of large ion orbits [7, 31], toroidicity [32] and thermal plasma pressure gradient [33]. In plasma with higher pressure, the deformation of the continuum itself becomes important due to the geodesic acoustic effect [34]. This deformation will be described later, but it is important to note here that both $\Delta\omega$ and the geodesic acoustic contribution remain nearly constant on the time scale of $q_0(t)$ evolution.

Except in the vicinity of $q_{\mathrm{TAE}} \equiv (2m - 1)/2n$, each AC mode consists of predominantly one poloidal Fourier component.

As $q_0(t)$ approaches q_{TAE}, toroidicity-induced coupling modifies the dispersion relation (2.1) and changes the mode structure into a sum of two comparable harmonics (m and $m - 1$), as shown in figure 2. This transition from AC to TAE is seen as spectral line bending in figure 1 near the TAE gap. The corresponding theory has been developed in [32].

It is observed experimentally that the edge magnetic probe signals from the AC perturbations peak when the AC frequency enters the TAE gap (see, e.g. [30, 35]). This peaking can be reasonably attributed to radial broadening of the AC mode during its transition to TAE (as seen from the plots shown in figure 2). It is noteworthy that the mode can look stronger on the magnetic probes even when internal (reflectometer) measurements show that its amplitude decreases in the plasma core [30]. The change in the mode structure correlates with the change in the mode damping rate during the AC-to-TAE transition [36]. The AC-to-TAE transition
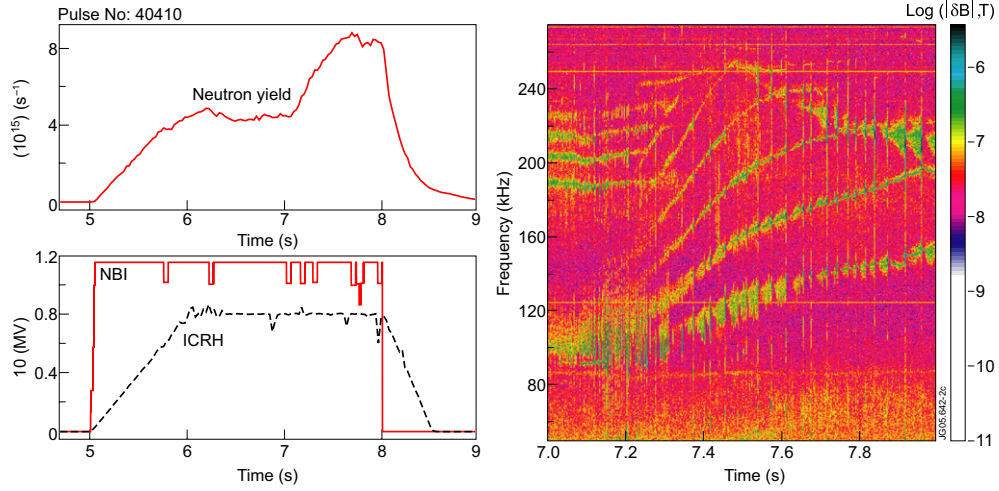
4

Figure 3. Left: neutron yield, NBI and ICRH power in JET discharge #40410 with toroidal magnetic field $B_T = 3.4$ T and plasma current $I_p = 3$ MA. Right: grand cascade observed at the time of the neutron rate and T_e increase [21].

is also accompanied by notable redistribution of the fast ions [35], although ACs themselves cause a weaker than TAEs degradation of fast-ion confinement. The relatively weak effect of the ACs on the fast-ion redistribution can be explained by the AC mode structure: the ACs with different mode numbers are all associated with the same magnetic flux surface at $q_0(t)$ and are localized in the vicinity of the zero shear point.

It follows from equation (2.1) that the AC frequency tracks the evolution of $q_0(t)$ so that the modes with higher poloidal numbers m have steeper slopes in figure 1. The sequence of modes in figure 1 is also consistent with (2.1): each mode appears when $q_0(t)$ passes a corresponding rational value m/n. The integer values of $q_0(t)$ give rise to so-called *grand cascades* in which there are simultaneous unstable modes with all toroidal mode numbers, such as in figure 1 at $t \approx 5.2$ s. This clustering of the ACs has been employed in MHD spectroscopy to find the exact timing of the safety factor evolution [8, 9, 21].

On JET, the excitation of ACs is observed in almost every reversed-shear discharge with ICRH or NBI, but these modes do not cause significant degradation of fast-ion confinement in JET plasmas. On the other hand, the measured discrete spectrum of ACs provides valuable information about both fast ions and MHD characteristics of plasmas. A particularly important example is the relation between the grand cascades, integer values of $q_0(t)$, and so-called ITB triggering events [21, 37]. This relation has been first observed on JET, and it is presented in figure 3. As seen from the figure, the neutron rate in the discharge is constant for about one second (from $t = 6$ s to $t = 7$ s) at a fixed power of NBI and ICRH. However, the yield then goes up and almost doubles after $t = 7$ s without any change in the NBI or ICRH power. At the same time, a grand cascade is detected by Mirnov coils, which indicates that the safety factor $q_0(t)$ takes an integer value at the location of magnetic shear reversal.

In order to investigate the correlation between ACs and ITBs with higher time resolution and a higher degree of certainty, a technique of AE detection from plasma density perturbations has been developed [12]. Figure 4 shows an example of the O-mode interferometry (top) versus Mirnov coils measurements of the same ACs (bottom). Other types of interferometry measurements, e.g. the far infrared (FIR) interferometry, used for density measurements
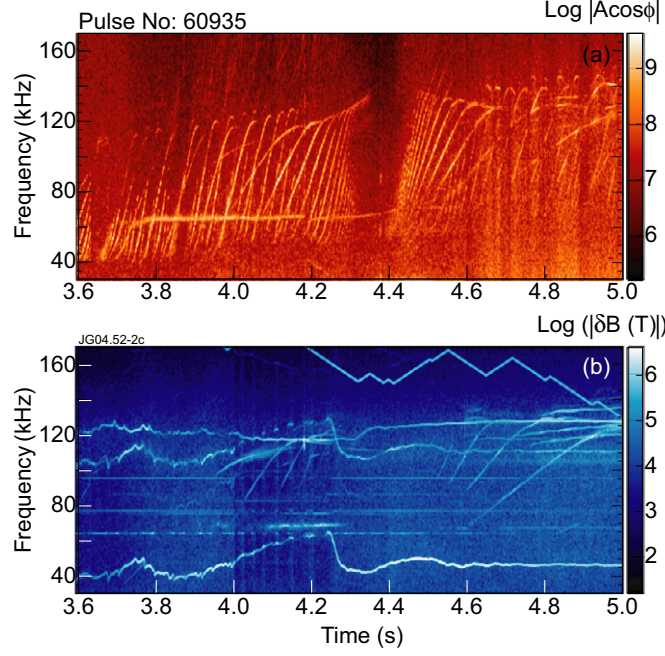
Figure 4. ACs detected in the same discharge with O-mode interferometry (top) and with Mirnov coils (bottom). Microwave beam frequency 45.2 GHz was just above the cut-off frequency of the O-mode [12]. Reprinted with permission from [12]. Copyright 2011 by the American Physical Society.

also detect high-frequency modes, and these now operate successfully on JET [21] and on DIII-D [13, 38].

With the newly developed diagnostic technique, numerous JET reversed-shear experiments have demonstrated a close link between ITBs and integer values of $q_0(t)$ [21]. The ITB triggering event is observed on the electron temperature profile $T_e(r; t)$ as a spontaneous steepening of the slope $\partial T_e/\partial r$ when $q_0(t)$ approaches/passes an integer value. Figure 5 shows an example of such an event with constant heating power applied.

The steepened electron temperature profile either relaxes in a few hundred milliseconds or develops into an ITB if the main heating power is being supplied when the triggering event occurs. Figure 6 shows a grand cascade soon *after* the ITB triggering event. A similar sequence of events is observed in most of the discharges not perturbed by strong MHD phenomena such as NTM [21]. This sequence suggests that the spontaneous improvement in electron confinement is likely to be associated with a gap in the density of the rational surfaces prior to the appearance of an integer q_0 [39] rather then with the very existence of an integer q_0 in the plasma [37]. The link between ITB triggering and low-order rational surfaces inferred from the grand cascades is routinely used on JET for developing ITB scenarios in the following way. A single discharge with low power ICRH is performed first at the beginning of an experimental session and the times of AC appearance are accurately measured. Thanks to the very good reproducibility of JET discharges, the measured times for the grand cascades with low-order rational values of q_0 are then used reliably in all other discharges of the series to turn on the main heating power at a desirable 'target' value of q_0 in order to create an ITB [21, 37]. The correlation between ITB triggering events and ACs has also been seen clearly in DIII-D [38]. It was, however, noted that such a link seems to weaken in discharges with higher plasma density.

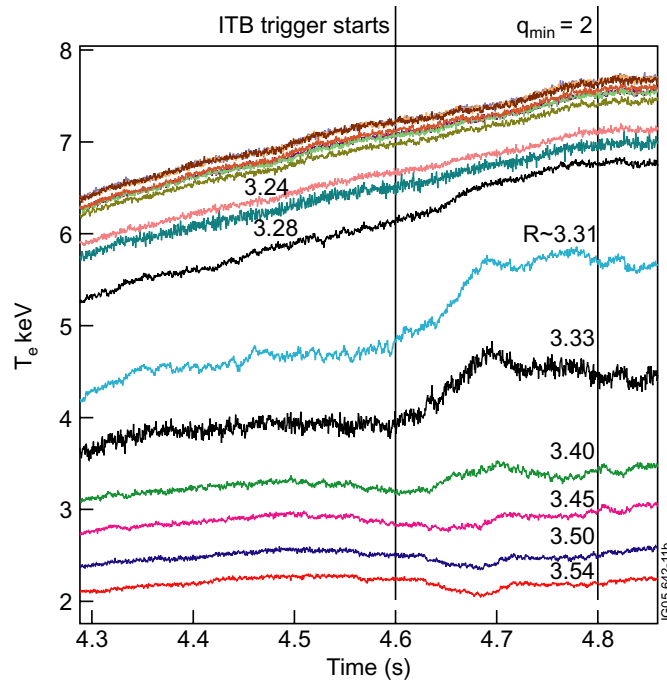**Figure 5.** Electron temperature traces measured with multi-channel ECE in JET discharge #61347. An ITB triggering event is seen at $t = 4.6$ s [21].
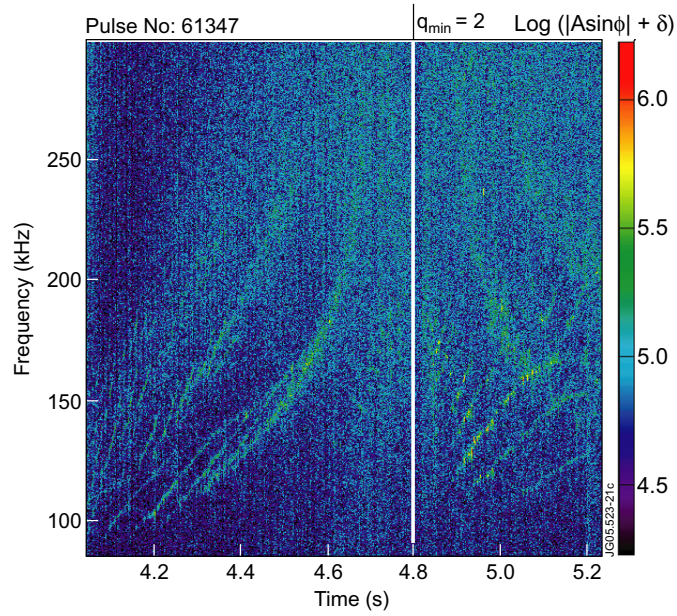

Figure 6. ACs detected with O-mode interferometry in JET discharge #61347. Due to the Doppler shift nf_{ROT} in this toroidally rotating plasmas the discrete spectrum observed spreads over a broad frequency range. A grand cascade is seen at $t = 4.8$ s [21].

We now note an interesting difference between the AC spectrograms in figure 4 (top) and in figure 6. This difference results from fast toroidal rotation of the plasma in the discharge shown in figure 6. The plasma spins up due to the uni-directional NBI. The mode frequency f_n^{LAB} in the laboratory reference frame differs from the frequency f_n^0 in the plasma reference frame by a Doppler shift,

$$f_n^{\text{LAB}} = f_n^0 + n f_{\text{rot}}(r_0), \tag{2.2}$$

where $f_{\text{rot}}(r_0)$ is the rotation frequency at the mode location and n is the toroidal mode number. With increasing toroidal rotation of the plasma, the Doppler shift modifies the frequency of AC significantly. However, the grand cascade is still seen clearly in this case in figure 6 as a bunch of modes starting at the same time but with frequencies separated by the Doppler shifts.

Measurements of ACs on DIII-D, made with FIR interferometry, [40] give somewhat different spectrograms than those on JET. The Doppler shift was about 20% of the TAE frequency in DIII-D (due to the strong $E \times B$ rotation) and it had the opposite sign. The competition between the negative Doppler shift and the upward frequency sweeping due to the time-dependent safety factor $q_0(t)$ forms a 'hilly' structure of the AC spectral lines seen in figure 7.

2.2. Quasimodes

The preferred upward direction of AC sweeping seen in figure 1 indicates that a Schrodinger-type equation for the AC has a radial potential well for the upward sweeping eigenmodes, as opposed to a potential hill for the downward sweeping perturbations [41]. However, in some JET discharges with weakly reversed $q(r)$ profile (about 1% of total number), ACs can also sweep downwards and exhibit frequency rollover as shown in figure 8. This rollover indicates a hill-to-well transition for ACs.

The rollover and the downward sweeping can be interpreted in terms of AC quasimodes that arise on the potential hill and stay there transiently prior to damping at the Alfvén continuum resonance. The fairly large value of the lowest frequency in figure 8 results from the deformation of the shear Alfvén continuum due to the geodesic acoustic effect [34]. In the limit of large mode numbers n and m, both AC modes and quasimodes are governed by the same wave equation

$$\frac{\partial}{\partial r} \left[\omega^2 - \omega_{\text{G}}^2 - \frac{V_{\text{A}}^2}{R^2} \left(n - \frac{m}{q} \right)^2 \right] \frac{\partial \Phi}{\partial r} - \frac{m^2}{r^2} \left[\omega^2 - \omega_{\text{G}}^2 - \frac{V_{\text{A}}^2}{R^2} \left(n - \frac{m}{q} \right)^2 - \omega_{\nabla}^2 \right] \Phi = 0, \tag{2.3}$$

where $\omega_{\text{G}}^2 \equiv (2/MR^2)(T_{\text{e}} + \frac{7}{4}T_{\text{i}})$ is the square of the geodesic acoustic frequency and

$$\omega_{\nabla}^2 \equiv -\frac{2}{MR^2} r \frac{\text{d}}{\text{d}r}(T_{\text{e}} + T_{\text{i}}) - \frac{\omega}{m} \left| \frac{eB}{Mc} \right| \frac{r}{n_{\text{plasma}}} \frac{\text{d}}{\text{d}r} \langle n_{\text{fast}} \rangle$$

is an offset arising from the plasma pressure gradient and from the fast-ion response in the large orbit limit. Assuming that the perturbation of interest is localized near the zero shear point r_0 such that $|r - r_0| \ll r_0$, one can expand the safety factor $q(r)$ around r_0 and look for a radially extended solution of (2.3) with $(r_0/m) \ll |r - r_0| \ll r_0$. This requires that ω^2 be very close to

$$\omega_0^2 \equiv \omega_{\text{G}}^2 + \frac{V_{\text{A}}^2}{q_0^2 R^2}(nq_0 - m)^2 + \omega_{\nabla}^2. \tag{2.4}$$
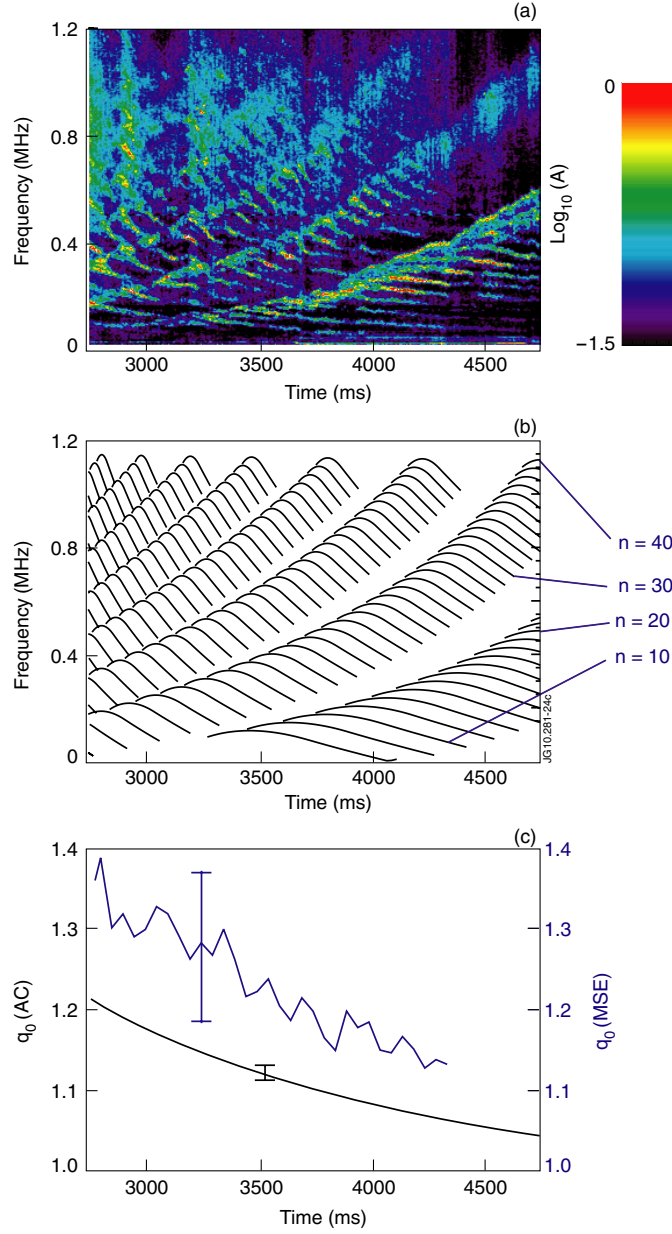
Figure 7. Top: evolution of the FIR scattering spectrum showing ACs in the DIII-D discharge. Middle: model analysis of frequency evolution of Alfvén continuum at q_0 indicating toroidal mode numbers in the range from 8 to 40. Bottom: time evolution of q_0 inferred on DII-D from ACs and measured with MSE (Reprinted with permission from [40]. Copyright 2011 by the American Physical Society).

One can then neglect small radially dependent quantities in the second derivative term of (2.3). With these simplifications, (2.3) reduces to

$$\frac{\partial^2 \Phi}{\partial z^2} = [\lambda - \eta z^2 - z^4]\Phi, \tag{2.5}$$
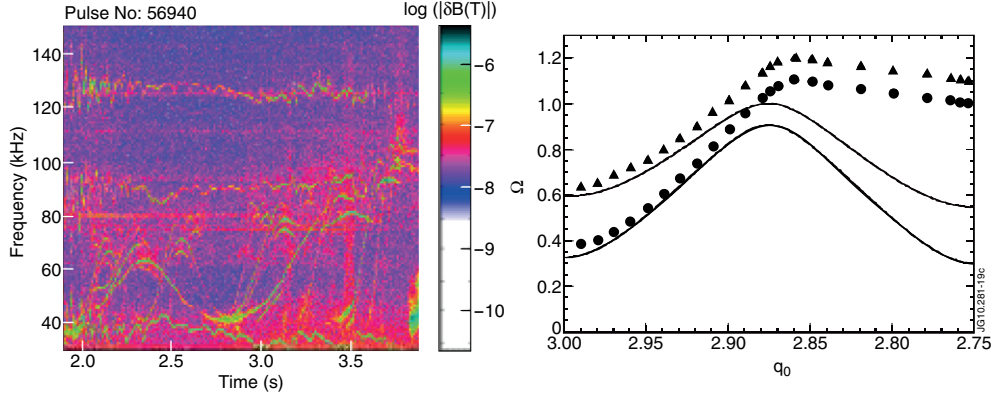
Figure 8. Left: magnetic spectrogram showing ACs in JET discharge #56940. ACs with different toroidal mode numbers reach the same lowest frequency. Right: Alfvén spectral line behaviour computed from theory [34], showing the effect of pressure on the mode frequency as a function of safety factor q_0. Reprinted with permission from [34]. Copyright 2011, American Institute of Physics. The solid curve represents the MHD continuum, and the triangular and the circular points are for $\beta = 0.005$ and $\beta = 0.0015$, respectively.

where

$$z \equiv \frac{r - r_0}{r_0} \left[\frac{V_A^2}{\omega_\nabla^2 q_0^2 R^2} \left(\frac{mnr_0^2 q_0''}{2} \right)^2 \right]^{1/6}$$

is a dimensionless radial coordinate and η and λ are dimensionless parameters defined as

$$\eta \equiv (nq_0 - m) \left(\frac{2m^2}{nr_0^2 q_0''} \frac{V_A^2}{\omega_\nabla^2 q_0^2 R^2} \right)^{1/3}, \qquad \lambda \equiv \frac{\omega^2 - \omega_0^2}{\omega_\nabla^2} \left(\frac{\omega_\nabla R}{V_A} \frac{2q_0}{r_0^2 q_0''} \right)^{2/3} \left(\frac{m^2}{n} \right)^{2/3}.$$
(2.6)

The upward sweeping AC modes are solutions of (2.5) with $\eta < 0$, whereas AC quasimodes represent solutions with $\eta > 0$ and with radiative boundary conditions at infinity. Let $\lambda(\eta)$ be a complex eigenvalue of (2.5) for $\eta > 0$. Of particular interest is the eigenvalue with the lowest imaginary part, corresponding to the weakest damping. In the limit of large η, i.e. when q_0 is sufficiently far from the m/n rational surface, (2.5) reduces to the Schrödinger equation for an inverted pendulum [41]. The characteristic lifetime of the quasimode wave-packet can then be calculated analytically. The corresponding damping rate for large η is [42]

$$\gamma(\eta) = -\sqrt{\eta} \cdot \left(1 - \frac{3}{4} i \eta^{-3/2} + \frac{21}{16} \eta^{-3} \right) \frac{\omega_\nabla^2}{2\omega_0} \left(\frac{V_A}{\omega_\nabla R} \frac{r_0^2 q_0''}{2q_0} \right)^{2/3} \left(\frac{n}{m^2} \right)^{2/3}.$$
(2.7)

The opposite limiting case of small η refers to perturbations near the rational magnetic surface with $q_0 = m/n$. In this limit, one can set $\eta = 0$ in (2.5) to obtain:

$$\frac{\partial^2 \Phi}{\partial z^2} = (\lambda - z^4) \Phi.$$
(2.8)

The least damped quasimode solution of (2.8) has $Im\lambda \approx 0.57$, with the following dependence of the damping rate on plasma parameters:

$$\gamma_{\eta=0} = -\frac{0.57}{2} \sqrt{\omega_G^2 + \omega_\nabla^2} \left(\frac{\omega_G^2}{\omega_G^2 + \omega_\nabla^2} \frac{V_A}{R\sqrt{\omega_G^2 + \omega_\nabla^2}} \frac{r_0^2 q_0''}{2q_0} \right)^{2/3} \left(\frac{1}{mq_0} \right)^{2/3}.$$
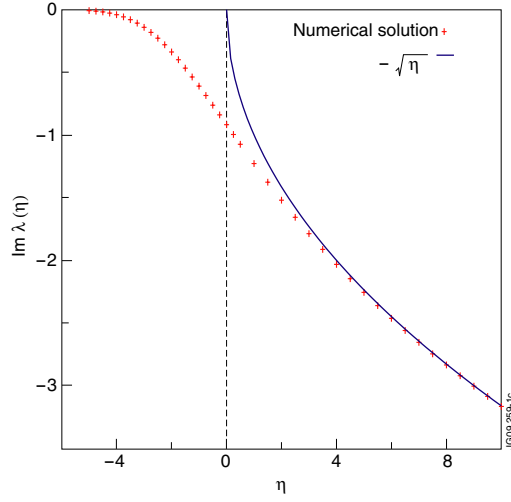(2.9)

10

Figure 9. Numerical solution for the dimensionless damping rate $Im\,\lambda$ compared with the analytical result for large η. Reprinted with permission from [42]. Copyright 2011, American Institute of Physics.

For intermediate values of η, a time-dependent Schrödinger equation was solved numerically [42] to give the dimensionless damping rate $Im\,\lambda$ shown in figure 9.

A population of ICRH-accelerated ions can provide sufficient drive to overcome the quasimode damping. Calculation of this drive requires a non-perturbative treatment described in [42]. In the high-n limit, the dominant contribution to the particle-to-wave power transfer comes from the turning points regions of the fast-ion banana orbits. As a result, despite the large width of the fast-ion orbits, the ensuing wave equation retains the Schrodinger-type structure, rather than becoming an integro-differential equation. An interesting difference between the 'true' modes and quasimodes is that the 'true' modes have a rigid structure due to discreteness of their frequencies whereas rigidity of the quasimodes is due to quantization of their damping rates.

It is important to note that radiative damping of quasimodes can also be viewed as a result of phase mixing between different kinetic modes that make up the initial perturbation. As an alternative to a single radiatively damped quasimode, one can consider a dense spectrum of kinetic Alfvén modes for which finite Larmor radius (ρ_i) effects create a potential well to form bound states [43, 44]. The frequency spacing $\delta\omega$ for these discrete kinetic modes is given by [43]

$$\frac{\delta\omega}{\omega_0} = 2\rho_i \sqrt{\frac{T_e}{T_i} + \frac{3}{4}} \sqrt{\frac{q_0''}{q_0}} \left(\frac{nq_0}{m} - 1\right)^{-1/2}. \tag{2.10}$$

By comparing this spacing with the quasimode damping rate (2.7) in the limit $\eta \gg 1$, which refers to the commonly observed flattish q-profiles, we find that the damping rate exceeds the spacing if

$$\frac{r_0}{\rho_i m} \frac{\omega_\nabla}{\omega_0} > 1. \tag{2.11}$$

This inequality makes it allowable to ignore discretization of the kinetic mode spectrum, because the timescale required to resolve the neighbouring kinetic modes is longer than $1/\gamma_d$ by which time the quasimode has either decayed to zero or grown beyond the applicability of
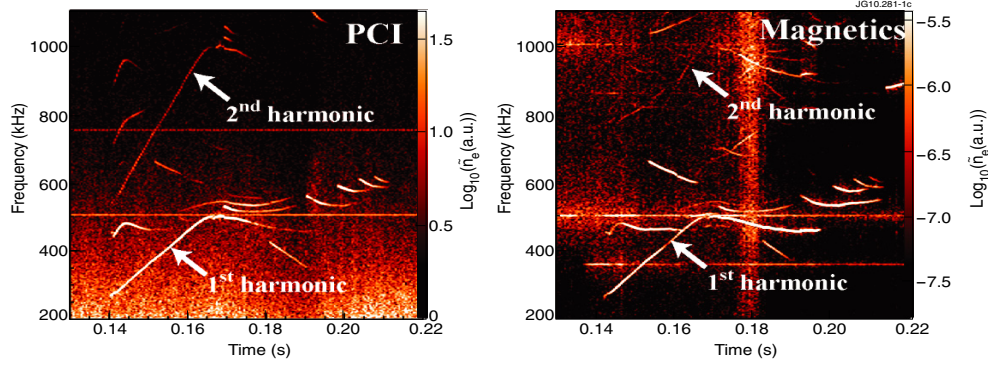
Figure 10. The second harmonic of AC and TAE is observed in Alcator C-MOD [14] on the PCI diagnostic (left) and hardly seen on the magnetic pick-up coils (right). Reprinted with permission from [14]. Copyright 2011, American Institute of Physics.

linear theory. Near marginal stability, i.e. for the case $\gamma_L - \gamma_d \ll \gamma_d$, where γ_L is the linear drive due to resonant particles, an extra factor $(\gamma_L - \gamma_d)/\gamma_d$ appears in equation (2.11), which makes criterion (2.11) more restrictive. Violation of this criterion means that the kinetic modes become distinguishable. Such modes with a broad radial scale have been constructed in [44].

2.3. Nonlinear sidebands and internal measurements

As seen from (2.4), the measured deviation of the AC frequency from the idealized dispersion relation (2.1) can apparently be used to determine the ion temperature, the electron temperature or fast-ion parameters, depending on which contribution dominates in (2.4). Another interesting opportunity for plasma diagnostics involves nonlinear sidebands of Alfvén eigenmodes. In experiments on Alcator C-MOD [14], measurements of density fluctuations with PCI in figure 10 show a second harmonic of the basic AC and TAE signals. This second harmonic perturbation can be interpreted as a nonlinear sideband produced by the eigenmode via quadratic terms in the MHD equations [45]. The signal at 2ω is nearly resonant with the $(2m; 2n)$ branch of the Alfvén continuum.

The resulting enhancement of the second harmonic is counteracted by the relatively weak nonlinearity of the shear Alfvén waves. For shear Alfvén perturbations in a uniform equilibrium magnetic field, the quadratic terms $4\pi\rho(\mathbf{v}\cdot\nabla)\mathbf{v}$ and $(\mathbf{B}\cdot\nabla)\mathbf{B}$ tend to cancel in the momentum balance equation. For this reason, special care is needed to include magnetic curvature effects properly and to evaluate the coupling between shear Alfvén perturbations and compressional perturbations. As shown in [45], the ratio of the second harmonic density perturbation $\rho_{2\omega}$ to the first harmonic perturbation ρ_ω is roughly $\rho_{2\omega}/\rho_\omega \approx mq_0(R/r_0)(|\delta B_\omega|/B_0)$, where $|\delta B_\omega|$ is the perturbed magnetic field at the fundamental frequency. This estimate is consistent with recent new measurements on Alcator C-MOD [46]. The estimate for $\rho_{2\omega}/\rho_\omega$ can be refined via more detailed calculations, which would provide the spatial structure of the second harmonic signal for the observed modes. Such calculations together with PCI data would then allow the determination of the perturbed fields inside the plasma, rather than just at the plasma edge as with magnetic probes.

Internal measurements of mode amplitude and mode structure have been boosted in experiments on various machines recently. The mode structure diagnostic is based on measurements of electron density perturbations. The density perturbation δn, created in a tokamak by plasma displacement ξ in a shear Alfvén wave, contains a convective part and a
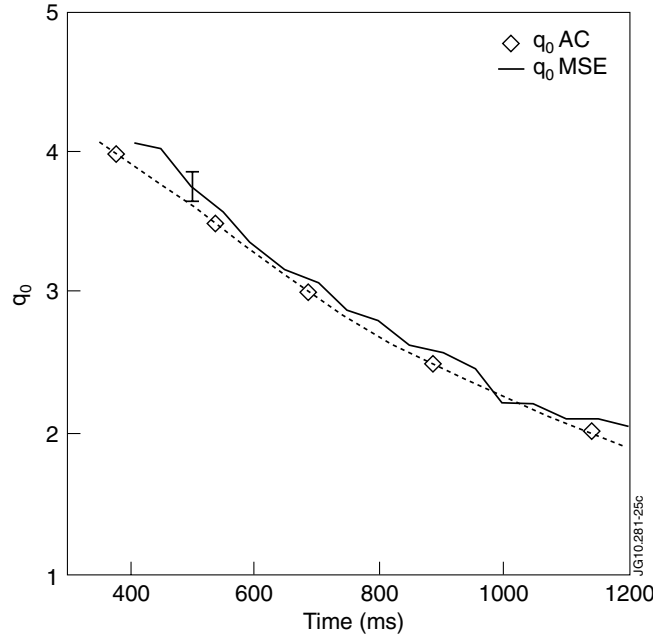
Figure 11. Minimum safety factor as a function of time for DIII-D discharge 123202. The solid line is the MSE derived value (with a typical error bar shown). Diamonds indicate the minimum safety factor inferred from AC (RSAE) measurements. Errors on AC-derived timing are roughly estimated to be the width of the diamond markers (± 5–10 ms) [48].

compressional part [47],

$$\frac{\delta n}{n_0} = -\xi \cdot \frac{\nabla n_0}{n_0} - \nabla \cdot \xi \cong -\left(\frac{\nabla n_0}{n_0} + \frac{2\boldsymbol{R}}{R^2}\right) \cdot \xi.$$

The convective contribution to δn is due to the equilibrium density gradient ∇n_0, whereas the compressional contribution is associated with the geodesic curvature $\kappa \equiv \boldsymbol{R}/R^2$, where $\boldsymbol{R}/R$ is the unit vector along a major radius direction and R is the major radius. In the case of ACs, the density perturbations measured by the X-mode reflectometry reveal mode localization and thereby identify the location of magnetic shear reversal. This diagnostic technique has been used extensively on DIII-D [48] and JET [15]. A more recent PCI diagnostics on C-MOD [49] enhances this capability.

Based on a model for the AC frequency, a sensitive diagnostic for the evolution of the minimum magnetic safety factor $q_0(R, t)$ was developed and compared successfully with motional Stark effect (MSE) measurements, an example of which for DIII-D is shown in figure 11.

The successful use of 'Alfvén spectroscopy' on present-day machines has demonstrated the importance and feasibility of the core diagnostic of AEs in ITER [1]. With regard to ITER, this technique of monitoring temporal evolution of the safety factor profile can serve as a back-up to the MSE diagnostic. On C-MOD, the PCI measurements over a wide width in major radius have led to an excellent technique of reconstructing the AE mode structure [49]. Figure 12 shows an example of such reconstruction and comparison with the NOVA code modelling. In this case, the effect of cancellation of positive and negative density perturbations along the line-of-sight was investigated in detail.
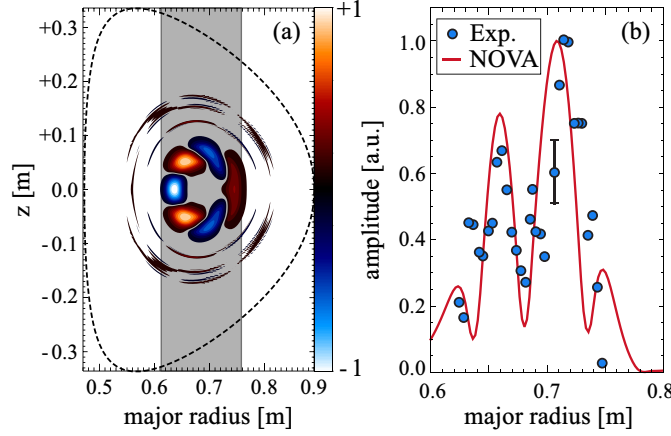
Figure 12. (*a*) The two-dimensional density perturbation calculated by NOVA. The shaded area indicates the PCI viewing region. (*b*) The synthetic PCI data are compared with the experimental data, showing overall good agreement between the structures [49]. Reprinted with permission from [49]. Copyright 2011 by the American Physical Society.

Finally, excellent internal diagnostics of AEs has been developed on DIII-D [50] based on ECE measurements. The multiple-channel ECE technique expands the capability of mode detection significantly due to its high spatial resolution. The ECE technique is one of the main diagnostics for equilibrium temperature measurements, and multiple ECE channels are already available for that. The use of ECE as a diagnostic for AEs requires only a modest amendment: digitization of the measured signals up to the relevant frequency range.

3. Nonlinear evolution of energetic-particle-driven mode

The near-threshold regimes of wave excitation by energetic particles reveal a rich family of nonlinear scenarios ranging from benign mode saturation to spontaneous formation of nonlinear coherent structures (phase-space holes and clumps) with time-dependent frequencies [22–25, 51, 52]. This variety results from an interplay between the wave field, which tends to flatten the distribution of resonant particles, and the relaxation processes, which tend to restore the unstable distribution function. The relaxation process was modelled in [22] via an 'annihilation' (Krook [53]) collision operator. Within this model, four regimes of the near-threshold evolution of a single wave have been predicted depending on the ratio of the effective relaxation rate ν_{eff} to the linear growth rate γ: (1) a steady-state regime; (2) a regime with periodic amplitude modulation; (3) a chaotic regime and (4) an 'explosive' regime. The case of velocity-space diffusion exhibits very similar nonlinear behaviour [51, 52].

The first three regimes have been identified in JET experiments on TAE excitation by ICRH (ion cyclotron resonance heating) [23, 24]. The explosive regime leading to a strongly nonlinear phase was identified in MAST experiments with TAEs driven by NBI [25]. Due to the strong nonlinearity that develops in the explosive scenario, the instability on MAST was observed in the form of TAE 'bursts', representing a near-threshold type of a general 'bursting' nonlinear scenario described in [54].

Figure 13 illustrates observations of different nonlinear scenarios. Experimentally, the TAEs driven by ICRH-accelerated ions on JET exhibit a variety of regimes just above the excitation threshold. Figure 13 shows how raw signals and magnetic spectrograms of TAE change during gradual increase in ICRH power [24]. In this case, the distribution function of
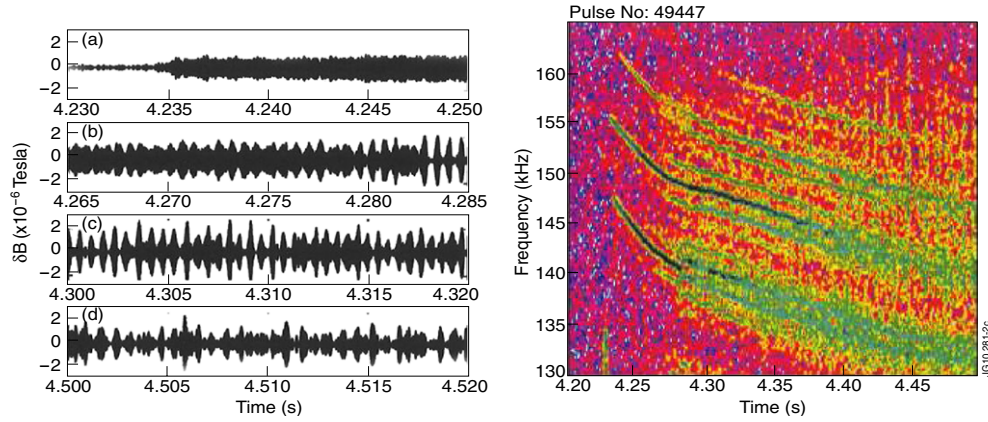
Figure 13. At gradually increasing ICRH power, TAEs exhibit steady state, periodically modulated, and chaotic regimes. The left panel shows the magnetic probe signals. The right panel shows magnetic spectrograms obtained via Fourier decomposition of the signals. Reprinted with permission from [24]. Copyright 2011 by the American Physical Society.
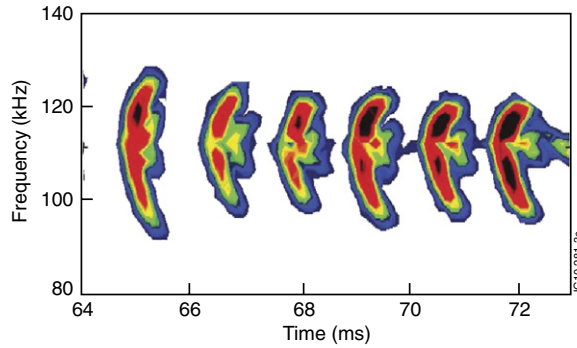

Figure 14. NBI-driven bursting TAEs on MAST [25].

the fast ions resonating with TAEs is formed via quasilinear RF diffusion. The effective rate of replenishing the distribution function, ν_{eff}, is therefore an order of magnitude higher than the rate associated with Coulomb collisions [23]. In agreement with the theory [23, 24], such a diffusion-dominated distribution function gives a soft nonlinear regime of TAE with steady or modulated amplitude. Although the diffusive case does not exclude a hard nonlinear regime with the explosive TAE evolution, such regimes are rare in experiments.

On the other hand, the nonlinear TAE driven by NBI-produced energetic ions on MAST, very rarely exhibit a steady-state nonlinear evolution. Most often, the explosive regime is observed that gives a bursting evolution of the mode amplitude with a sweep in the mode frequency. Figure 14 shows an example of such a TAE-bursting mode [25].

These findings suggest that the difference between the JET and MAST observations may be due to specifics of the fast-particle relaxation mechanisms. Consequently, the earlier theoretical model has been generalized by including dynamical friction (drag) as an additional relaxation mechanism. The upgraded model has revealed that only the explosive behaviour is possible in the near-threshold regime when drag dominates over other relaxation mechanisms [55]. As a result, the instability follows a so-called 'hard' nonlinear scenario in which the saturation level

is insensitive to the initial linear growth rate. This profound difference in behaviour arises due to a qualitative change in the nonlinear response of the system from an exponential 'loss of memory' to an oscillatory response with positive nonlinear feedback.

Technically, the near-threshold regimes are described by the following cubic nonlinear equation for normalized mode amplitude A:

$$\frac{dA}{d\tau} = A(\tau) - \frac{1}{2} \int_0^{\tau/2} dz z^2 A(\tau - z)$$
$$\times \int_0^{\tau - 2z} dx \, \exp[-\hat{\nu}^3 z^2 (2z/3 + x) - \hat{\beta}(2z + x) - i\hat{\alpha}^2 z(z + x)]$$
$$\times A(\tau - z - x) A^*(\tau - 2z - x) \tag{3.1}$$

where the time τ is measured in the units of the linear instability growth time. The quantities $\hat{\nu}$, $\hat{\beta}$ and $\hat{\alpha}$ represent the rates of velocity-space diffusion, annihilation and drag, respectively, (normalized to the instability growth rate). The dimensionless amplitude A is proportional to the perturbed field and its normalization depends on a specific mode of interest. Equation (3.1) implies that the characteristic bounce frequency ω_b of resonant particles trapped by the mode is

$$\omega_b = |A|^{1/2} \gamma (\gamma/\gamma_d)^{1/4} \tag{3.2}$$

where γ_d is the mode damping rate in the absence of energetic particles, and the ratio γ/γ_d is much smaller than unity, because the energetic-particle drive only slightly exceeds the background damping γ_d in the near-threshold regime.

Equation (3.1) determines whether the initial linear instability evolves into a soft or hard nonlinear regime. The amplitude A saturates at a finite level in the soft case, whereas the hard case gives a solution that 'explodes' in a finite time. In the absence of drag ($\hat{\alpha} = 0$), (3.1) admits a saturated solution in which $|A|^2 = 2[\int_0^\infty (z^2 \, dz/\hat{\beta} + \hat{\nu}^3 z^2) \exp(-2\hat{\nu}^3 z^3/3 - 2\hat{\beta}z)]^{-1}$ at $\tau \to \infty$, and the amplitude indeed converges to that solution, but only when the annihilation rate ($\hat{\beta}$) and/or diffusion rate ($\hat{\nu}$) are sufficiently large. At smaller values of $\hat{\beta}$ and $\hat{\nu}$, the steady saturated solution is unstable, which gives rise to a periodic limit-cycle behaviour known as 'pitchfork splitting'. Further decrease in the relaxation rates creates period doubling bifurcations and then leads to a chaotic mode amplitude evolution and to explosive growth of the mode. The details of these transitions can be found in [22, 23]. The same (3.1) also shows that the mode evolution is always explosive in the case of pure drag ($\hat{\beta} = \hat{\nu} = 0$). The cubic nonlinear term in the equation is destabilizing in this case. Because of that (3.1) does not have any saturated solution at ($\hat{\beta} = \hat{\nu} = 0$), and the mode grows beyond the applicability range of (3.1).

In the presence of both drag and diffusion, the existence of steady saturated solutions is only prohibited when the integral in (3.1) has a negative real part at $\tau \to \infty$, which takes place at $\hat{\nu}/\hat{\alpha} < 1.043$ (as marked by the dashed line in figure 15). However, some of the steady solutions that formally exist at $\hat{\nu}/\hat{\alpha} > 1.043$ are in fact unstable [55]. The stability boundary is shown in figure 15 by the solid line. The area above the solid line represents stable steady solutions.

Equation (3.1) implies that the dominant nonlinear effect from the wave is modification of the resonant particle drive whereas the background damping is herein assumed to be linear. In particular, this model applies to the case in which the background damping is purely collisional and does not involve any resonant phenomena. Yet, in reality, the damping mechanism itself may also be of resonant nature, like Landau damping on plasma particles or continuum damping. The wave can then modify both the drive and the damping. Moreover, a nonlinear reduction of the damping rate may actually enhance the instability as it happens in fishbone pulses (see section 4). Equation (3.1) allows a straightforward generalization to describe this
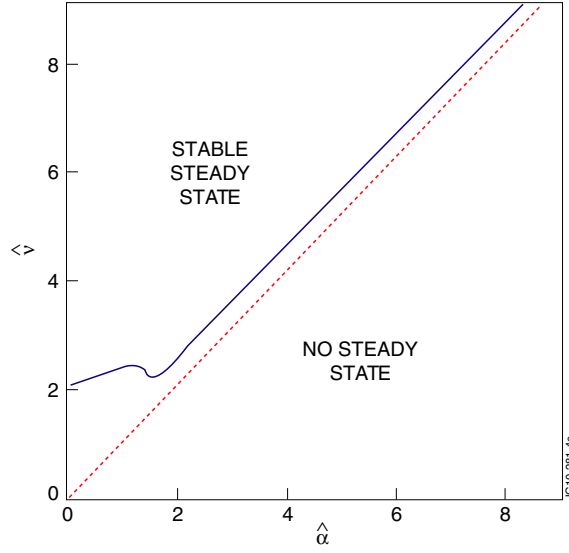
Figure 15. Displays the boundaries in parameter space that give stable, unstable and no steady-state solutions to (3.1). The unstable solution lies in between the solid and dashed lines. Reprinted with permission from [55]. Copyright 2011 by the American Physical Society.

interplay of different resonances [61] in the near-threshold regime. Alternatively, the resonance that is responsible for wave damping may still behave as a linear resonance if a sufficiently fast classical relaxation rate prevents its nonlinear distortion (this can happen because the effective collision frequencies are generally different for different resonances).

In order to apply the above scenarios to the TAE instability in toroidal geometry, one needs to consider a group of particles that resonate with the wave. The corresponding resonance condition is $\omega - n\langle\omega_\phi\rangle - l\langle\omega_\theta\rangle = 0$, where ω is the TAE frequency, $\langle\omega_\phi\rangle \equiv \langle d\phi/dt\rangle$ and $\langle\omega_\theta\rangle \equiv \langle d\theta/dt\rangle$ are the orbit frequencies of energetic ions along the toroidal, ϕ, and poloidal, θ, coordinates, $\langle\cdots\rangle$ represents the orbit averaging, n is the toroidal mode number of the TAE, and l is an integer value. The particles detune from the resonance due to the drag and diffusion, and the appropriate collision operator for the problem is a Fokker–Plank operator written in action angle variables. Its explicit form, which can be found in [52], allows one to express the quantities $\hat{\nu}$ and $\hat{\alpha}$ in terms of plasma parameters and thereby evaluate the relative importance of pitch-angle scattering and slowing down for the resonant ions.

Observations of TAEs on different machines have shown that there is a tendency for NBI-driven Alfvénic instabilities to exhibit a bursting behaviour (hard nonlinear regime) on NSTX [11], TFTR [4], DIII-D [5] and JT-60U [56]. On the other hand, ICRH-driven modes, similar to those observed in JET [23, 24], show predominantly soft regimes on TFTR [57], JT-60U [58], DIII-D [59] and C-MOD [14]. Taking into account that the distribution function of NBI-produced ions establishes itself due to electron dynamical friction, while the distribution function of ICRH-accelerated ions is formed via a quasilinear diffusive process, we find that the difference in observed nonlinear scenarios is consistent with the trend predicted by (3.1).

The explosive near-threshold regimes are known to give rise to phase-space holes and clumps. The build-up of such structures was demonstrated in [60, 61], but their initial quantitative description was limited to the case of small frequency deviations from the bulk plasma eigenfrequency. However, there are multiple experimental observations of frequency-sweeping events in which the change in frequency is comparable to the frequency itself
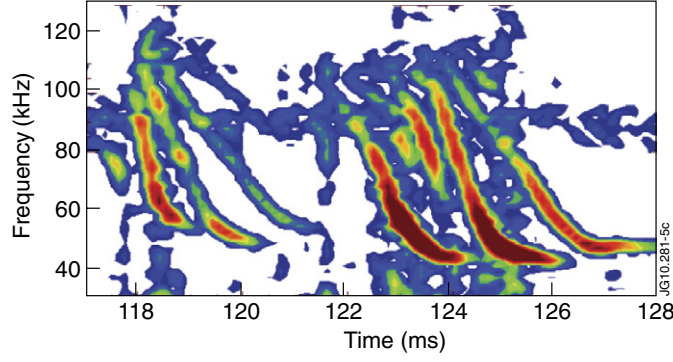
17

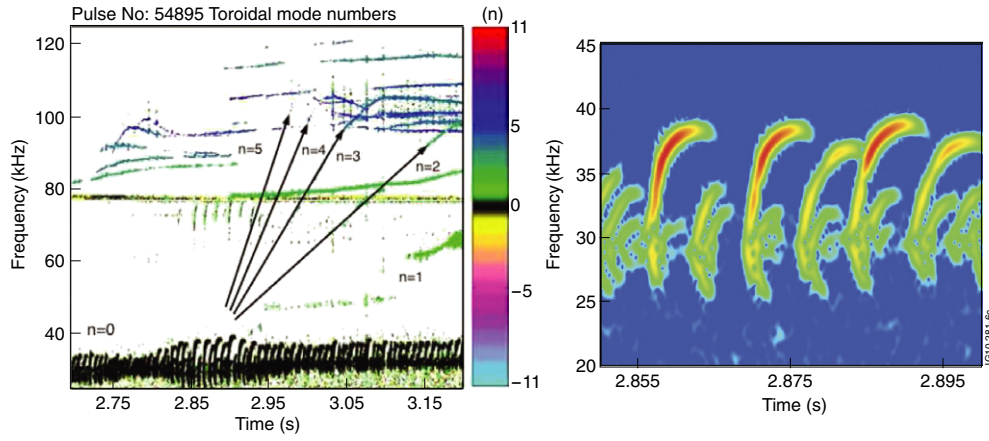**Figure 16.** NBI-driven chirping modes on MAST [10].

Figure 17. Left: phase magnetic spectrogram showing modes with various toroidal mode numbers excited by ICRH in JET discharge #54895. The $n = 0$ mode is seen at around 30 kHz and marked in black. ACs are seen in the range 40–110 kHz. Right: the $n = 0$ mode in #54895 (zoom) [65].

[10, 62, 63]. Figure 16 shows an example of such 'chirping' frequency modes with downward frequency sweeping observed in MAST discharges with NBI-heating [10].

Another example is modes with upward frequency sweeping observed in JET discharges with high field side ICRH (i.e. the ICRH resonance layer is on the high field side from the magnetic axis of the tokamak). Figure 17 shows persistent, high clarity, upward frequency chirping modes with toroidal mode number $n = 0$ [64, 65]. These oscillations have frequency just below the lowest AC frequency, and they obey the $T_e^{1/2}$ scaling typical of geodesic acoustic mode (GAM) [66]. Therefore, these modes were identified as energetic-particle-driven global geodesic acoustic mode (GGAM) [64], which are electrostatic at the main localization region, but become electromagnetic away from it. The free energy source driving these modes is found to be associated with the bump-on-tail energy distribution function created by ICRH.

Interpretation of such dramatic phenomena as the ones in figures 16 and 17 requires a non-perturbative theoretical formalism developed recently in [67]. The underlying idea is that coherent structures with varying frequencies represent nonlinear travelling waves in fast-particle phase space. Given that the energetic-particle density is usually much smaller than the bulk plasma density, it seems difficult for these particles to change the eigenmode frequency

significantly. The way to resolve this difficulty is to take into account that regardless of how small is the energetic-particle density, a coherent group of these particles can still produce an observable signal with a frequency different from the bulk plasma eigenfrequency. A relevant example is a modulated beam in the plasma. The modulation occurs spontaneously as a result of the initial instability and resonant particle trapping by the excited wave. The initial modulation matches the frequency of a plasma eigenmode. However, as the coherent structure evolves due to dissipation, the trapped particles slow down without losing coherency, and the resulting frequency shifts considerably from the initial frequency. The corresponding theoretical building block is then a nonlinear Bernstein–Greene–Kruskal (BGK) mode [68], rather than a slowly evolving plasma eigenmode. In [67], a rigorous solution of this type has been obtained for a simple one-dimensional bump-on-tail model with immobile ions and with the following form of the perturbed electrostatic potential φ:

$$\varphi \equiv -\frac{1}{|e|}U[x - s(t); t] \tag{3.3}$$

where e is the electron charge, and the electron potential energy U is a periodic function of its first argument $[x - s(t)]$ and a slowly varying function of the second argument t. Also, the wave phase velocity $\dot{s} \equiv \mathrm{d}s(t)/\mathrm{d}t$ is a slowly varying function of time with a sweeping rate $\ddot{s}$. The perturbed cold electron density is linear in φ whereas the density perturbation of the fast electron tail is nonlinear, dominated by the adiabatic response of the trapped particles. Evaluation of this nonlinear response involves the notion that the electron distribution function is nearly uniform within the trapped particle phase-space area and that the ambient passing particles are basically unperturbed.

The resulting Poisson equation for the BGK mode has the form

$$\frac{\partial^2 U}{\partial z^2} = -U\omega_{\mathrm{p}}^2/\dot{s}^2 - \{8\pi e^2\left[f_0(\dot{s}_0) - f_0(\dot{s})\right]\sqrt{2/m}\}[\sqrt{(U_{\max} - U)} - \langle\sqrt{(U_{\max} - U)}\rangle], \tag{3.4}$$

where $z \equiv x - s(t)$, ω_{p} is the plasma frequency $\dot{s}_0$ is the initial phase velocity of the wave, f_0 is the unperturbed velocity distribution of the fast electrons, and angular brackets denote averaging over the spatial period λ. Equation (3.4) gives the following structure for the BGK mode [67]:

$$U = \frac{m\dot{s}^2}{2}\left\{\frac{32\pi e^2\dot{s}[f_0(\dot{s}_0) - f_0(\dot{s})]}{3m\omega_{\mathrm{p}}^2\cos\alpha}\right\}^2$$

$$\times\left\{\frac{1 + 2\cos^2\alpha}{2} - \frac{3\sin 2\alpha}{4\alpha} - \left[\cos\alpha - \cos\frac{2\alpha z - \alpha\lambda}{\lambda}\right]^2\right\}$$

$$\alpha \equiv \omega_{\mathrm{p}}\lambda/4\dot{s}. \tag{3.5}$$

For small deviations of $\dot{s}$ from $\dot{s}_0$ (early phase of frequency sweeping), (3.5) simplifies to

$$U = \frac{m\dot{s}_0^2}{4}\left\{\frac{32}{3\pi^2}\frac{\gamma_{\mathrm{L}}}{\omega_{\mathrm{p}}}\right\}^2\cos\left(\frac{2\pi z}{\lambda}\right), \tag{3.6}$$

where

$$\gamma_{\mathrm{L}} \equiv \omega_{\mathrm{p}}\frac{\pi}{2n_0}\dot{s}_0^2\frac{\partial f_0(\dot{s}_0)}{\partial\dot{s}_0} \tag{3.7}$$

is the fast electron contribution to the mode growth rate. Equation (3.6) reproduces the result of [60], i.e. a sinusoidal mode with constant amplitude at the beginning of frequency
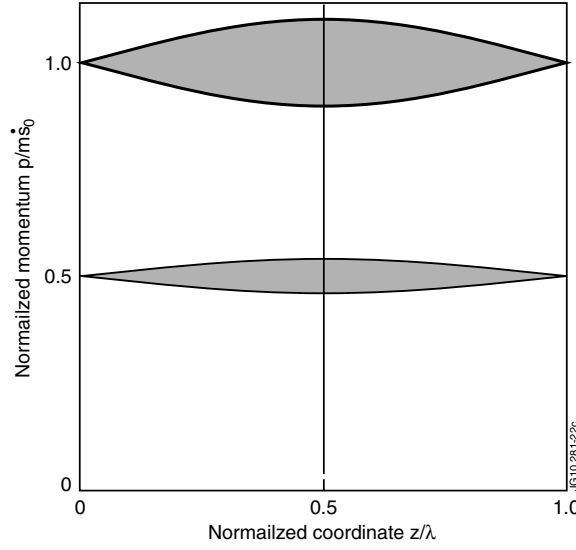
Figure 18. Evolution of the phase-space bucket during the sweeping event. The plot shows the initial separatrix (upper shaded area) and the shrinked separatrix at half of the initial mode phase velocity (lower shaded area).

sweeping. On the other hand, the more general expression (3.5) shows that the amplitude and the mode structure change significantly for larger variations of $\dot{s}$. As a result, the boundary (separatrix) between the passing and trapped particles changes its shape as shown in figure 18. The separatrix shrinks and thereby releases some of the originally trapped particles, like a leaking phase-space bucket. The remaining particles move to lower velocities together with the separatrix, which allows the wave to extract power from the fast-particle population. The extracted power is

$$P = -[f_0(\dot{s}_0) - f_0(\dot{s})]2m\dot{s}^2\lambda \left| \frac{32\pi e^2\dot{s}[f_0(\dot{s}_0) - f_0(\dot{s})]}{3m\omega_p^2\cos\alpha} \right| \left[\frac{\sin\alpha}{\alpha} - \cos\alpha \right] \frac{d\dot{s}}{dt} \tag{3.8}$$

and the balance between this power and the power dissipated in the bulk plasma determines the rate of sweeping needed to compensate for collisonal dissipation of the BGK mode.

Early in time, the power balance condition gives

$$\frac{d}{dt} \frac{(\dot{s} - \dot{s}_0)^2}{\dot{s}_0^2} = \frac{\nu}{3} \left| \frac{16\gamma_L}{3\pi^2\omega_p} \right|^2, \tag{3.9}$$

where ν is the cold electron collision frequency. This expression reproduces the square root scaling of frequency sweeping found in [60]. Later in time, the mode moves further away from the initial linear eigenmode, and its phase velocity $\dot{s}$ deviates gradually from the simple square root scaling.

This evolution can be viewed as spontaneous transformation of the initial plasma wave into an energetic-particle mode. It also presents a plausible scenario for energetic-particle modes generated by Alfvén wave instabilities [69–71], for which nonlinear modification of the mode structure appears to be essential, especially when the instability is non-perturbative even in the linear regime.

The presented consideration of the 1D electrostatic bump-on-tail problem suggests a similar approach to the frequency-sweeping events in tokamaks. Experimentally, such events can be attributed to the excitation of weakly unstable Alfvén waves. However, the measured
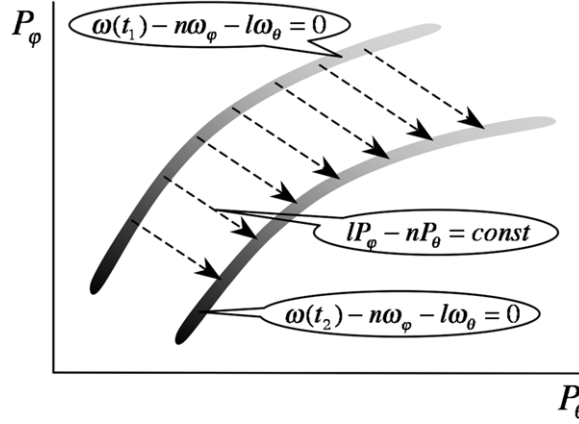
Figure 19. Transport of resonant particles during frequency sweeping. The shaded areas are snapshots of the moving resonant region in the momentum space. The shades of grey mark different values of the particle distribution function. The trapped resonant particles form a locally flat distribution across the resonance and preserve the value of their distribution function when the resonance carries them along the dashed lines.

frequency quickly moves away from the original eigenmode frequency, and a plausible underlying mechanism is spontaneous formation of coherent phase-space structures at the wave–particle resonances.

For a linear mode, the resonance condition has the form

$$\omega - n\omega_\varphi(P_\varphi; P_\theta; P_\psi) - l\omega_\theta(P_\varphi; P_\theta; P_\psi) = 0, \tag{3.10}$$

where ω is the mode frequency, $\omega_\varphi(P_\varphi; P_\theta; P_\psi)$ and $\omega_\theta(P_\varphi; P_\theta; P_\psi)$ are the toroidal and poloidal transit frequencies, and n and l are integers. The pairs $(P_\varphi; \varphi)$, $(P_\theta; \theta)$ and $(P_\psi; \psi)$ are the canonical action-angle variables for the integrable unperturbed motion. The third pair $(P_\psi; \psi)$ describes fast gyro-motion that does not resonate with shear Alfvénic perturbations. For an isolated linear resonance, the perturbed particle Hamiltonian is a sinusoidal function of $\omega t - n\varphi - l\theta$. Similarly to the bump-on-tail problem, transition to the nonlinear case generalizes the Hamiltonian to

$$H = H_0 + U\left(\int_0^t \omega(\tau)\,\mathrm{d}\tau - n\varphi - l\theta; t\right), \tag{3.11}$$

where the function U (to be determined numerically) is still a periodic (but not necessarily sinusoidal) function of its first argument. We now note that the quantities P_ψ and $P = lP_\varphi - nP_\theta$ are constants of motion for such a Hamiltonian and that slow evolution of the function U should also preserve an adiabatic invariant for trapped particles. These three conservation laws establish a simple relationship between the trapped particle distributions at any two locations of the resonance (see figure 19).

The distribution of the ambient passing particles remains virtually unperturbed. Any macroscopic quantity, such as perturbed energetic-particle pressure, now becomes a known functional of the unperturbed distribution and the 'potential energy profile' U. What remains to be solved (numerically) is a set of linear MHD equations for bulk plasma response with an analytic nonlinear input from the energetic particles. These equations represent an analogue of (3.4), and their solution determines the wave profile U. After that, the power balance condition can be used to calculate the frequency-sweeping rate.
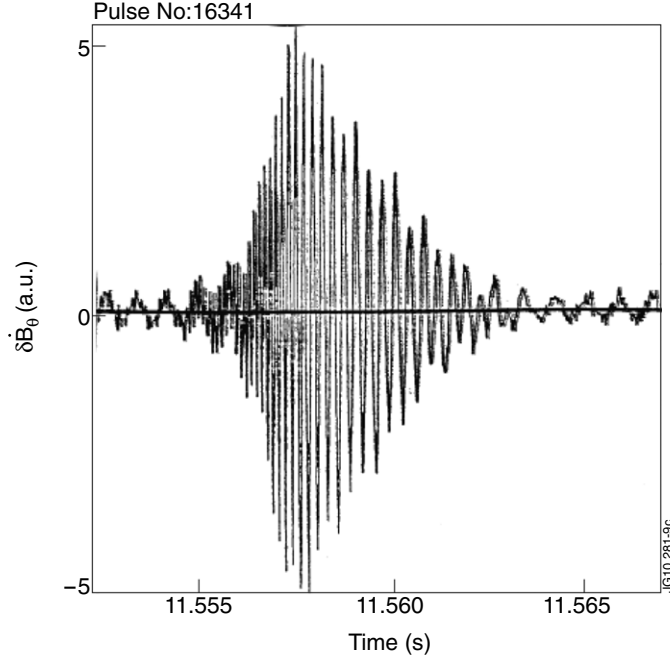
Figure 20. Oscillations of the perturbed magnetic field time derivative during fishbone burst (JET discharge #16341) [74].

4. The fishbones

A bursty 'fishbone' instability, with toroidal mode number $n = 1$ and dominant poloidal mode number $m = 1$, was first observed in experiments with perpendicular NBI on the Poloidal Divertor Experiment (PDX) tokamak [72] and then found in most tokamaks with a suprathermal ion population: DIII-D [73], JET [74], JT-60U [75], ASDEX-U [76] and MAST [77]. Figure 20 shows a typical fishbone burst signal from a Mirnov coil. The repetitive bursts resemble fish skeletons going one-by-one, hence the name 'fishbones' given to such oscillations. The fishbone instability is known to cause enhanced losses of energetic ions. It may also thwart confinement of the thermal plasma by initiating long-lasting kink and neoclassical tearing modes [76–78].

The fishbone bursts are oscillatory. Their frequency typically decreases by about a factor of two during each burst as can be seen, e.g. from figure 20. Experimentally, the radial plasma displacement in the fishbone mode was found to have a 'top-hat' structure of the internal $n = 1$ kink mode [79] associated with the $q = 1$ magnetic surface, where q is the safety factor. The frequency of the fishbone oscillations in PDX was found to be close to the magnetic precession frequency of the trapped energetic ions, $\langle \omega_{dh} \rangle$, as well as to the thermal ion diamagnetic frequency, ω_{*pi}. The original theoretical interpretation [80] established the resonant wave–particle interaction at $\omega = \langle \omega_{dh} \rangle$, as the key drive for the fishbone instability. Two different regimes have been identified for the linear instability. The first regime of so-called 'precessional' fishbones [80] refers to the case when the mode frequency ω in the plasma reference frame is much greater than the thermal ion diamagnetic frequency, ω_{*pi},

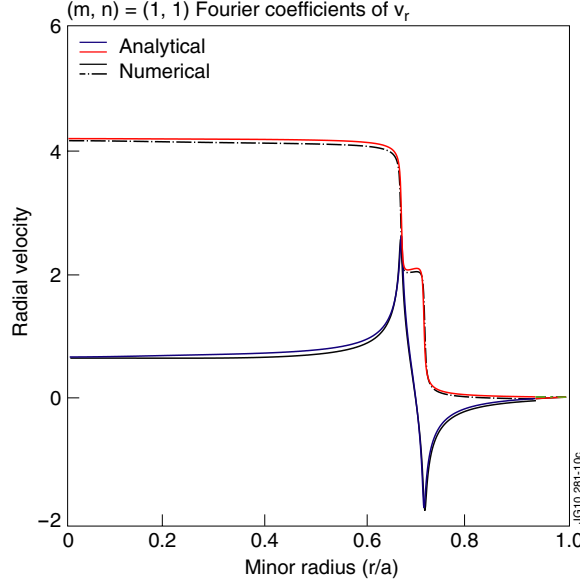$$\omega \gg \omega_{*pi}. \tag{4.1}$$

Figure 21. Spatial structure of the fishbone perturbation in the near-threshold regime. The real and imaginary parts of the radial velocity profile show two well-separated resonant sub-layers near the $q = 1$ surface. The width of each sub-layer is proportional to the mode growth rate. The distance between the sub-layers is proportional to the mode frequency.

In this case, trapped energetic ions destabilize the $n = 1, m = 1$ mode that emerges from the Alfvén continuum and is subject to continuum damping. At the onset of the fishbone pulse, the linear drive from fast particles is almost balanced by continuum damping near the $q = 1$ resonant surface. The mode structure shown in figure 21 has singularities at the radial locations, r_A, of Alfvén resonances,

$$\omega = \pm k_\parallel(r_A) V_A(r_A) \tag{4.2}$$

where $V_A(r)$ is the Alfvén velocity and $k_\parallel$ is the wave-vector parallel to the equilibrium magnetic field $\boldsymbol{B}_0$. Due to the significant continuum damping, associated with magnetic shear at the fluid resonances, the precessional fishbones are excited at relatively high values of the energetic (hot) ion beta, $\beta_{\mathrm{hot}} \equiv 4\pi P_{\mathrm{hot}}/B_0^2 > \beta_{\mathrm{hot}}^{\mathrm{crit}}$. Here P_{hot} is the pressure of energetic ions and the threshold value $\beta_{\mathrm{hot}}^{\mathrm{crit}}$ is determined by the balance between the kinetic drive due to the energetic ions, γ_{hot}, and the Alfvén continuum damping, γ_{MHD}, which can be expressed in the form

$$\Gamma \equiv \frac{\gamma_{\mathrm{hot}}}{\gamma_{\mathrm{MHD}}} = 1. \tag{4.3}$$

The precessional fishbones constitute an example of the hard nonlinear excitation scenario due to the destabilizing dependence of the threshold parameter Γ on the wave amplitude.

The second linear regime refers to the fishbones with $\omega \approx \omega_{*\mathrm{pi}}$ [81, 82]. In this case, the mode lies within a low-frequency gap in the Alfvén continuum, which effectively eliminates continuum damping. In this regime, the fishbones represent one of the two FLR-stabilized oscillatory kink modes which would be unstable within ideal MHD [83].

Numerous fishbone experiments on various machines have triggered a further significant development of the linear theory of fishbones. First, the theory of the energetic-particle drive for fishbones was extended in order to account for the transit resonances of the energetic

ions [84] and finite orbit width corrections [85]. Second, the impressive results obtained on STs required a careful analysis of instabilities in STs, and fishbones were one of the prominent avenues there.

In STs with tight aspect ratio and high volume averaged beta [86], the fishbone modes may differ significantly from those in large-aspect-ratio tokamaks. In particular, the fishbone drive from both trapped [87] and passing [88] energetic ions terminates if the equilibrium magnetic field B has a minimum in major radius. This happens at very high values of β, which can be achieved in STs due to improved MHD stability at tight aspect ratios. In the presence of radial minimum in B, the power transfer from trapped energetic ions to the mode becomes negative as its sign depends on the sign of $\partial B/\partial r$. On the other hand, the toroidal drift frequency, ω_{dh}, of the energetic passing ions becomes so large at high β that the drift motion shifts the radial location of the wave–particle resonance by several particle orbit widths [88]. This large orbit effect suppresses the instability drive from the passing ions.

Furthermore, the fishbone modes in STs may have a different radial mode structure than the conventional $q = 1$ fishbone. In particular, the very low magnetic shear, typical for ST plasmas, may permit an infernal $n = 1$ fishbone mode even at $q > 1$, or the structure of the fishbone mode may be similar to the interchange mode [89]. These specifics of STs still require simultaneous treatment of the MHD and wave–particle nonlinearities with regard to fishbones.

In addition to the ion-driven fishbones, there are also fishbone-like instabilities driven by energetic electrons. They were discovered in DIII-D experiments with ECRH [90] and more recently observed in other machines under ECRH and low hybrid heating. A nice overview of these instabilities and the related theoretical formalism can be found in [91]. It is noteworthy that, due to the smallness of electron drift orbits, the electron fishbones in present-day devices may replicate essential features of the ion-driven fishbones in large burning plasma experiments.

Losses of energetic ions resonating with the fishbones were examined in experiments on many machines. In the worst case scenario of plasmas with high-$\beta_{\mathrm{p}} \equiv 8\pi nT/B_{\mathrm{P}}^2$ (at small plasma current), when the fishbone amplitude is high and particle orbits are wide, such losses may affect the fast-ion population significantly. For example, losses of NBI-produced energetic ions in low current low field JET tritium discharges could exceed 50% of the total beam energy content [92]. The resonant redistribution/losses due to fishbones in burning plasmas of the ITER-scale machine were assessed in [83]. It was shown that typical energy range for resonant fusion born alpha particles is 300–400 keV, well below the birth energy 3.5 MeV. Losses of such ions due to fishbones may, in fact, be beneficial for ash removal from the plasma core.

Non-resonant losses of alpha particles with high energies were predicted in [83] as well. For very fast ions, the mode looks like a stationary $n = 1$ MHD perturbation of the plasma. This perturbation destroys the toroidal symmetry of the magnetic field and distorts the fast-ion trajectories (see, e.g., [93]). In particular, it broadens the regions of phase space corresponding to the unconfined orbits (prompt loss region), giving rise to enhanced non-resonant losses due to the $n = 1$ fishbone. Experimentally, the fishbone-induced non-resonant losses of highly energetic fusion products were detected on DIII-D, TFTR and JET [94–96].

The advancements of plasma scenarios reveal some new phenomena associated with fishbones, of which two cases of long-lasting MHD perturbations are of particular interest: (i) a long-living $n = 1$ kink modes in low-shear STs, e.g. MAST [77], and (ii) fishbone initiated NTMs in so-called 'hybrid' scenarios on JET [97] and ASDEX-U [76].

When fishbones initiate a long-living $n = 1$ kink mode in MAST (see figure 22), this mode sometimes becomes locked and provokes degradation of plasma confinement. The bursting fishbones seemingly evolve into steady-state long-living modes. This effect is likely to be
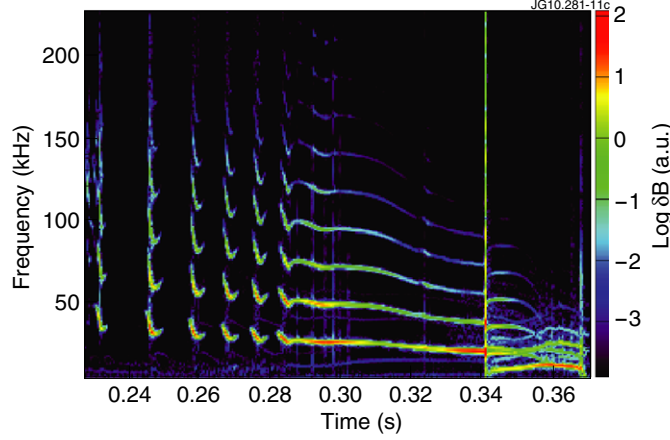
Figure 22. Magnetic spectrogram showing fishbone oscillations that initiate a long-living $n = 1$ kink mode (at frequency 30 kHz) in MAST discharge # 16038. The long-living mode degrades the plasma performance and causes internal reconnection event at $t = 0.34$ s.

associated with a gradual decrease in the safety factor q and radial expansion of the $q = 1$ surface. At small radii of the $q = 1$ surface, i.e. at early time in figure 22, the ion diamagnetic frequency ω_{*pi} is relatively small (due to the smallness of the ion pressure gradient near magnetic axis). In this case, the ion diamagnetic frequency is lower than the characteristic precessional frequency of the beam ions. As a result, the Chen–White–Rosenbluth fishbones [80] driven from the continuum are observed. As the $q = 1$ radius expands to the region with higher pressure gradient, the ion diamagnetic frequency ω_{*pi} increases, which is beneficial for the Coppi–Porcelli $\omega \approx \omega_{*pi}$ fishbones. It is therefore plausible that the observed initiation of a long-living $n = 1$ kink mode represents a gradual transformation of the Chen–White–Rosenbluth fishbones [80] into the Coppi–Porcelli mode [81], driven by the NBI-produced fast ions.

An interesting feature of the data shown in figure 22 is the presence of very high harmonics (up to seven) in the Mirnov coil signals. Such observations are very similar to so-called 'snake' MHD modes [98] which form a narrow helical current filament rotating toroidally. A possibility of the fishbones to form a current filament at the nonlinear phase of the mode development remains an intriguing open question.

In the development of a so-called 'hybrid' plasma scenario aimed at ITER [97], an important NTM triggering effect was observed during fishbone activity. A distinctive feature of this scenario is a broad region of flat $q(r)$ just above unity. The most common example of a reconnection in tokamak plasmas is the sawtooth reconnection driven by instability of the internal kink mode. However, experiments on ASDEX-Upgrade [76, 99] and on JET [97] have shown that fast-particle-driven fishbone instabilities, and frequency-sweeping modes in the Alfvén frequency range, can also initiate NTM reconnections. Figures 23 and 24 display a typical example of this kind on JET.

The interplay between the fishbones and long-living NTM on JET is somewhat more subtle than the initiation of the long-lasting $n = 1$ mode on MAST (figure 22). First, the $n = 2, m = 3$ NTM occurring at 28.8 s is localized near the $q = 3/2$ magnetic surface whereas the $n = 1$ fishbones are associated with the $q = 1$ magnetic surface. Second, the frequency coupling between the fishbone and the NTM appears to be due to differential toroidal rotation of the plasma, which allows the Doppler shift $nf_{rot}(q = 3/2)$ for the $n = 2$ mode
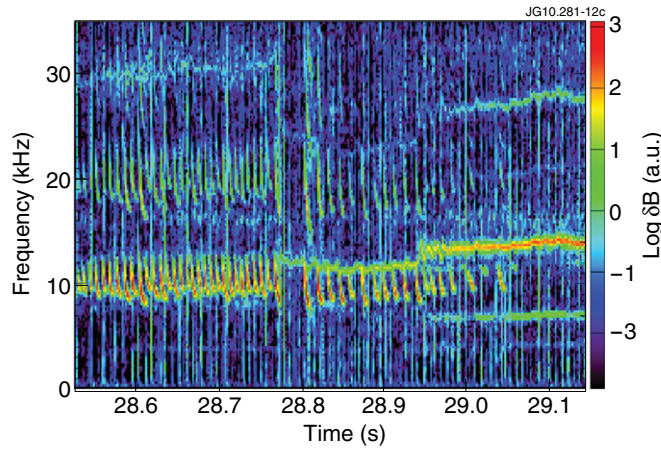
Figure 23. Magnetic spectrogram showing the typical JET hybrid scenario with $n = 1$ NBI-driven fishbones. Long-living NTM at frequency around 12–15 kHz (lab reference frame) is initiated in the absence of sawteeth or ELMs at $t = 28.77$ s and after some time it eventually degrades thermal plasma confinement.
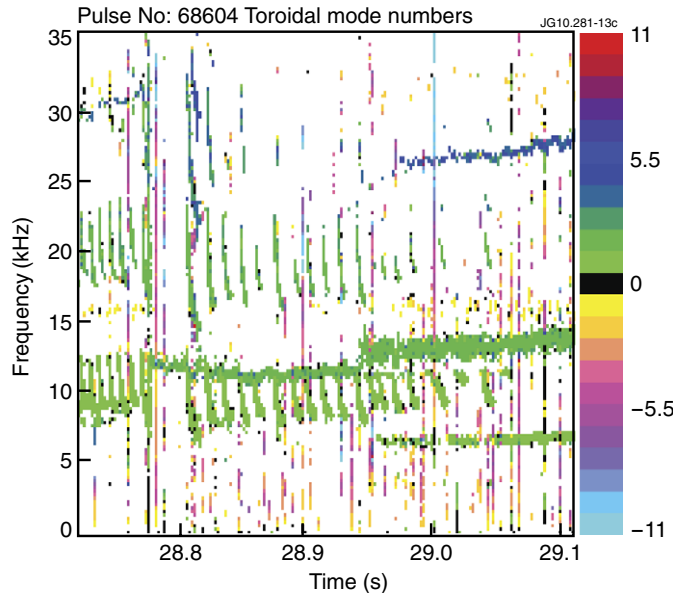

Figure 24. Magnetic spectrogram showing toroidal mode numbers of the perturbations in figure 23.

to match the Doppler-shifted fishbone frequency. It is also noteworthy that the excitation of NTM correlates with a change in the fishbones' period followed by suppression of fishbones after 29.05 s. However, the physics mechanism of the suppression is so far unclear.

A theoretical model for the observed NTM triggering by fishbones was recently proposed in [78]. The fishbones can act on the NTM as an external magnetic perturbation that brings the frequency of the micro-tearing islands into the unstable zone via toroidicity-induced coupling. The nonlinear equations for the NTM amplitude and phase contain a corresponding fishbone contribution. The role of fishbones is to kick off the NTM phase strongly enough to change the sign of the polarization current term in the NTM amplitude equation. It was also found

in [78] that multiplicity of the fishbone bursts may be essential, because a periodic sequence of small-amplitude bursts can move the NTM frequency into the unstable window easier than a single large burst.

The characteristic burst-like structure of the fishbone oscillations and the significant decrease in the oscillation frequency of the mode within a single burst indicate that fishbones have a strongly nonlinear character [100]. Significant progress was achieved in understanding the nonlinear evolution of the fishbones with the use of the nonlinear wave description very close to the instability threshold. Empirical nonlinear predator-prey models [100] as well as a more accurate model [51] were developed to interpret the repetitive bursts of the $\omega \approx \omega_{*\mathrm{pi}}$ fishbones and the resulting re-distribution of energetic ions. The model [51] based on the kinetic wave–particle trapping nonlinearity retains the essential physics of the $\omega \approx \omega_{*\mathrm{pi}}$ fishbones, since the kinetic nonlinearity appears to be the dominant one when the fishbones are in the diamagnetic $\omega_{*\mathrm{pi}}$ gap. This regime allows a perturbative description of the mode, which makes the problem technically similar to the bump-on-tail problem, as well as to many other wave–particle interaction problems (see [51] and references therein). For the $\omega \approx \omega_{*\mathrm{pi}}$ fishbone within the diamagnetic gap, the MHD damping effect is not important, $\gamma_{\mathrm{MHD}} = 0$, and kinetic damping due to thermal electrons and ions determines the excitation threshold instead. A linear theory of the kinetic damping for the $\omega \approx \omega_{*\mathrm{pi}}$ fishbones was developed by analogy with TAEs in, e.g., [101]. In nonlinear theory [51] such kinetic damping was considered to be of constant value not depending on the mode amplitude.

The description of precessional fishbones ($\omega \gg \omega_{*\mathrm{pi}}$) presents a more challenging problem as in this case γ_{MHD} becomes essential and the fluid resonances may behave strongly nonlinearly during the fishbone evolution. The linear responses from the kinetic and fluid resonances are almost equal near the instability threshold. However, their nonlinear responses are very different and a special investigation is needed in order to assess the importance of the fluid nonlinearity, in addition to the kinetic nonlinearity similar to the one analysed in [51].

The role of the fluid nonlinearity on the damping in the precessional fishbones was investigated in [26]. In order to delineate the effects of the fluid nonlinearity, a fishbone evolution was considered, during which the energetic ion response remained linear at all times so the effects of kinetic nonlinearity could be neglected.

The nonlinear MHD model for the fishbones [26] takes into account that fishbone modes are strongly extended along the equilibrium magnetic field, $k_{\parallel} \ll k_{\perp}$, so that the fast magnetosonic degrees of freedom, $\omega \cong k_{\perp} V_{\mathrm{A}}$, are not excited during the instability and the fishbone oscillations are of the shear Alfvénic type. It is important to note that the fluid nonlinearity, which is known to be small for local Alfvén waves satisfying the dispersion relation $\omega = k_{\parallel} V_{\mathrm{A}}$, is not small for the global fishbone mode that satisfies the condition $\omega = k_{\parallel} V_{\mathrm{A}}$ at two radial positions, $r = r_{\mathrm{A}}$, only. In order to exclude the magnetosonic oscillations, a nonlinear reduced MHD model [102, 103] combined with a linear response for the energetic particles was used in [26]. The analysis of the reduced MHD model for fishbones has shown that near the instability threshold, $\gamma_{\mathrm{hot}} - |\gamma_{\mathrm{MHD}}| \ll \gamma_{\mathrm{hot}}$, the radial structure of the fishbone mode of frequency ω has two singular layers, one inside and one outside the $q = 1$ surface as shown in figure 21. The radial locations, r_{A}, of the resonance layers are determined in accordance with

$$\omega^2 = (1 - q(r_{\mathrm{A}}))^2 [V_{\mathrm{A}}(r_{\mathrm{A}})/Rq(r_{\mathrm{A}})]^2. \tag{4.4}$$

Near the instability threshold of the fishbone, the radial width of each singular layer is smaller by a factor γ/ω than the distance between the layers, where $\gamma \ll \omega$ is the instability growth rate, $\gamma \equiv \gamma_{\mathrm{hot}} - |\gamma_{\mathrm{MHD}}|$.

Under these conditions, the fluid nonlinearity becomes important when the plasma displacement is comparable to the width of each singular layer near the $q = 1$ surface,
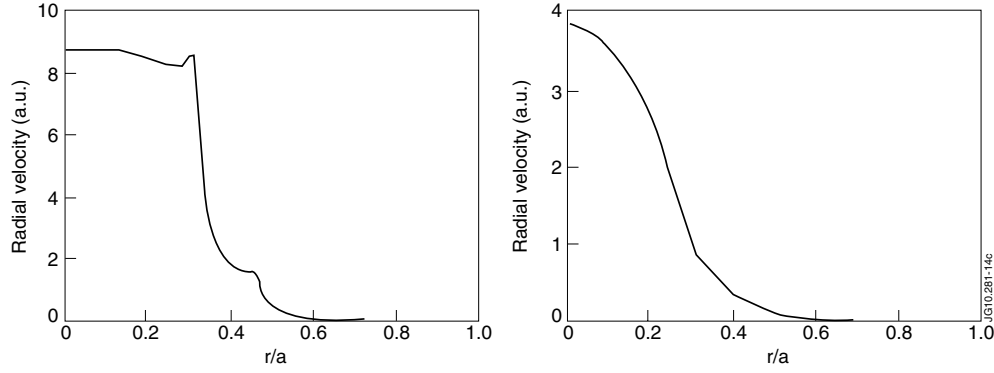
Figure 25. The radial velocity profiles in the linear (left) and nonlinear (right) regimes.

whereas the particle nonlinearity can still be negligible at this level. It was found in [26] that the dominant effects of the fluid nonlinearity in fishbones are caused by a generation of a $m = 0$ poloidal plasma flow, and a $m = 0$ poloidal magnetic field. The generation of the magnetic field, $\tilde{B}_p^{(0)}$, can be considered as a flattening of the 'effective' safety factor profile $q(r; t) = r B_T / R(B_p + \tilde{B}_p^{(0)})$.

The early stage of near-threshold fishbone instability, during which the two resonant layers are well separated, was found to be characterized by an explosive behaviour of the mode amplitude, accompanied by a fast change in the mode frequency and in the mode structure as shown in figure 25.

Fishbone events have long been recognized as a typical manifestation of so-called non-perturbative modes, for which the mode structure undergoes significant changes at the nonlinear stage. Although the overall top-hat structure of the fishbone is robust, a narrow resonant layer in the vicinity of the $q = 1$ surface dominates the nonlinear evolution of the mode, and one of the main challenges is to develop a credible description of that layer. The technical difficulties are most pronounced in the case of 'precessional' fishbones [80] because the case of 'diamagnetic' fishbones [81] still leaves room for a perturbative treatment.

A systematic nonlinear description of fishbones requires self-consistent treatment of kinetic and MHD nonlinearities, which is a challenging technical issue for numerical modelling. One of the difficulties here comes from the need to incorporate an accurate description of the narrow phase-space resonances into global MHD simulations. For linear problems, this difficulty is only a moderate obstacle since the resonant response of the system is often insensitive to the width of the resonance and can be treated in terms of Landau damping. In contrast, nonlinear problems typically need much better resolution to calculate the resonant response appropriately, which is prohibitively demanding for any of the existing global codes.

Several attempts have been made to address this issue. Two earlier efforts investigated the fishbone mode either using a nonlinear fast-particle pusher with linear MHD [104] or using a nonlinear MHD response with a linear description for energetic particles [26]. More recently, the approach of [104] was applied to electron-driven fishbones [91].

The full-geometry M3D code has both nonlinear MHD and nonlinear energetic particles, but encounters the resolution difficulty described above [105]. The challenge is to include kinetic phase-space resonances on an equal footing with fluid nonlinearities, while overcoming the resolution issue. This need is particularly evident for precessional fishbones.

Experimental data on precessional fishbones [72] exhibit a robust pattern with several elements that call for theoretical interpretation. These elements are (1) explosive initial growth

of the fishbone pulse, (2) saturation of the pulse, (3) downward frequency chirping during pulse decay and (4) recovery between subsequent pulses.

As already mentioned, at the onset of the fishbone pulse, the linear drive from fast particles is almost balanced by continuum damping near the $q = 1$ resonant surface. As the mode amplitude grows, the nonlinearity of the system becomes increasingly important. As can be seen from back-of-the-envelope estimates, the MHD nonlinearity initially dominates over the fast-particle nonlinearity. This early stage can be adequately described analytically within a weakly nonlinear approximation, which shows that the MHD nonlinearity plays a destabilizing role, leading to an explosive growth of the pulse [26]. The accelerated growth effectively broadens the two resonances shown in figure 25. The weakly nonlinear approximation holds as long as the two neighbouring resonances remain well separated. At the limit of its applicability the amplitude of the radial displacement ξ is on the order of $\xi \sim r_{q=1}\omega_{\text{th}}R/V_{\text{A}} \ll r_{q=1}$, where ω_{th} is the fishbone frequency at the excitation threshold. At this point the fast-particle nonlinearity is still negligible, so the particles continue to drive the mode. One can then expect that the mode will grow somewhat beyond the level of $\xi \sim r_{q=1}\omega_{\text{th}}R/V_{\text{A}}$ but the dynamics of this growth will now be different due to the non-perturbative nature of the MHD nonlinearity. It is conceivable that the structure of the MHD resonant layer will resemble a magnetic island of the kind described in [106] and the fast particles will force this island to grow until there is no free energy left in the fast-particle distribution. In other words, the growth of the fishbone pulse can only stop when the fast-particle nonlinearity flattens the phase-space distribution of particles near the kinetic resonance. Analytical theory has not yet been able to make credible predictions for the mode saturation level. Numerical simulations demonstrate mode saturation due to fast-particle nonlinearity, both with and without MHD nonlinearity in the code. However, numerical viscosity in the global nonlinear MHD code is currently too high to adequately describe the structure of the narrow resonant layer. We thus have an unresolved issue of predicting the mode saturation level in terms of plasma parameters and those of the fast particles.

The above description suggests that the mode saturates when the fast-particle drive switches off, due to nonlinear modification of the fast-particle distribution. Assuming that this modification is irreversible (due to fast-particle phase mixing), one can conjecture that the subsequent dynamics of the pulse should be similar to that of a nonlinear pendulum in the presence of dissipation. It is therefore natural that the mode frequency changes during the decay of the pulse since the frequency should depend on the mode amplitude. The fact that the frequency goes down can then be viewed as a reversal of the upward chirping predicted by the weakly nonlinear description of the explosive initial growth of the pulse [26]. A simple scaling argument suggests a quartic potential well for the fishbone-relevant pendulum. The reason is that the local Alfvén frequency is proportional to the distance from the $q = 1$ surface. For nonlinear perturbations, the characteristic distance is on the order of radial plasma displacement and it scales as the mode amplitude. We thus observe that the frequency of the relevant nonlinear pendulum should be proportional to the oscillation amplitude, which is indeed the case in a quartic potential well (figure 26).

In the light of the description above, it is interesting to note that the fishbone signals in figure 22 grow in amplitude during downward frequency sweeping. This is in contrast to the common case shown in figure 20 where the amplitude goes down together with the frequency. A plausible reason for the 'anomalous' mode evolution in figure 22 is low magnetic shear in the corresponding MAST discharges. Because of the low-shear, the continuum damping becomes quite small and the role of MHD nonlinearity should be less important. The overall fishbone dynamics could then be dominated by the wave–particle nonlinearity as opposed to fluid nonlinearity.
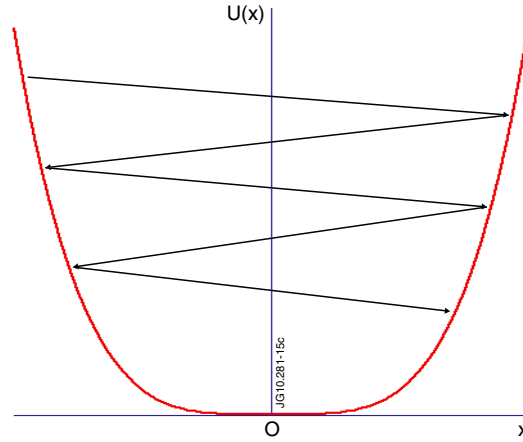
Figure 26. Damped oscillations in a quartic potential well illustrate nonlinear frequency downshift during fishbone pulse decay.

An additional open issue for fishbones is quantitative modelling of recurrent pulses in the presence of fast-particle sources and sinks. This problem is apparently more demanding computationally than the description of a single pulse because of the multiple time-scales that are involved.

We expect future theoretical studies of fishbones to provide a more complete picture of the near-threshold regime with an interplay between the kinetic and fluid nonlinearities. This research has an obvious linkage to MHD reconnection studies, which likewise deal with a boundary layer at a rational surface

5. Global transport of energetic particles

One of the main concerns about Alfvénic instabilities in fusion devices is that these instabilities may degrade confinement of the alpha particles and other fast ions and thereby forbid a self-sustained fusion burn. Each individual Alfvénic mode tends to be relatively benign in that regard. The reason is that the wave–particle resonances associated with a single low-amplitude mode can cover only a small fraction of the particle phase space. Consequently, many modes are needed to achieve resonance overlap in a sufficiently large area of phase space to give rise to global diffusion.

Particle diffusion over a set of overlapped resonances falls into the framework of quasilinear theory. In general, this diffusion breaks the constants of motion $(E; P_\varphi; \mu)$ that characterize unperturbed particle orbits. However, in the case of Alfvén modes, the particle magnetic moment μ still remains a good constant of motion. In addition, the particle energy remains nearly constant if the wave frequency is smaller than the multiples of the toroidal and poloidal particle frequencies in the resonant condition

$$\omega - n\omega_\varphi(E; P_\varphi; \mu) - l\omega_\theta(E; P_\varphi; \mu) = 0. \tag{5.1}$$

As a result, the waves affect predominantly the toroidal angular momentum P_φ or, equivalently, the radial position of the particle orbit in the poloidal cross-section of the tokamak. The width δP_φ of the resonance (5.1) can be roughly estimated as

$$\delta P_\varphi \frac{\partial}{\partial P_\varphi}[\omega - n\omega_\varphi(E; P_\varphi; \mu) - l\omega_\theta(E; P_\varphi; \mu)] = \omega_b, \tag{5.2}$$

where ω_b is the nonlinear bounce frequency for a resonant particle in the wave field.

The one-dimensional quasilinear diffusion equation in P_φ has the form

$$\frac{\partial f}{\partial t} - \frac{\partial}{\partial P_\varphi} D \frac{\partial f}{\partial P_\varphi} = -\nu(f - f_0), \tag{5.3}$$

where the right-hand side of the equation accounts for a Krook-type relaxation process and particle source that tend to establish a classical equilibrium distribution function f_0. The gradient of this distribution in P_φ provides an instability drive for the waves, with a linear growth rate $\gamma_0 = a(\partial f_0/\partial P_\varphi)$; the factor a depends on specifics of the modes that resonate with a given value of P_φ.

The diffusion coefficient D in (5.3) is proportional to the wave intensity and governed by the equation

$$\frac{\partial D}{\partial t} = 2\left(a \frac{\partial f}{\partial P_\varphi} - \gamma_d\right) D. \tag{5.4}$$

The background damping rate γ_d in this equation sets an instability threshold and is assumed to be smaller than γ_0.

In the absence of waves, the distribution function f will build up to $f \sim f_0 \sim (\gamma_0/a)P_\varphi$.

However, if the waves are present, the steady-state solution of (5.3) and (5.4) restricts f to $f \sim (\gamma_d/a)P_\varphi < f_0$. The corresponding diffusion coefficient can be estimated as

$$D \sim \frac{a}{\gamma_d}\nu f_0 P_\varphi \sim \nu \frac{\gamma_0}{\gamma_d} P_\varphi^2. \tag{5.5}$$

In order to formulate the resonance overlap constrain on the steady regime, we consider a set of barely overlapped resonances for which the correlation time is $1/\omega_b$ and

$$D \approx \omega_b(\delta P_\varphi)^2 \sim \omega_b^3 \frac{1}{\{(\partial/\partial P_\varphi)[\omega - n\omega_\varphi(E; P_\varphi; \mu) - l\omega_\theta(E; P_\varphi; \mu)]\}^2}. \tag{5.6}$$

This estimate can be rewritten as

$$D \approx (\delta P_\varphi)^3 \frac{\partial}{\partial P_\varphi}[\omega - n\omega_\varphi(E; P_\varphi; \mu) - l\omega_\theta(E; P_\varphi; \mu)]. \tag{5.7}$$

If the entire range of P_φ contains N resonant modes, then the overlap condition takes the form

$$D > \left(\frac{P_\varphi}{N}\right)^3 \frac{\partial}{\partial P_\varphi}[\omega - n\omega_\varphi(E; P_\varphi; \mu) - l\omega_\theta(E; P_\varphi; \mu)]. \tag{5.8}$$

We now observe from (5.5) and (5.8) that the resonance overlap condition requires a sufficiently strong source

$$\nu \frac{\gamma_0}{\gamma_d} > \frac{1}{N^3} P_\varphi \frac{\partial}{\partial P_\varphi}[\omega - n\omega_\varphi(E; P_\varphi; \mu) - l\omega_\theta(E; P_\varphi; \mu)]. \tag{5.9}$$

If the source is weaker than the value given by (5.9), then the global transport either terminates or becomes intermittent, depending on whether the individual modes can reach the overlap condition at some points in their nonlinear evolution. In the absence of overlap, the KAM surfaces between the resonances serve as transport barriers for fast particles. This brings an interesting question of whether such barriers can be created on purpose, especially at the plasma edge. Doing so may ensure satisfactory global confinement of fast particles even if there is a local instability in the core.

It is noteworthy that consideration of individually saturated modes gives a much more restrictive overlap condition than (5.9), namely

$$\gamma_0\left(1 + \frac{\nu}{\gamma_d}\right) > \frac{1}{N} P_\varphi \frac{\partial}{\partial P_\varphi}[\omega - n\omega_\varphi(E; P_\varphi; \mu) - l\omega_\theta(E; P_\varphi; \mu)]. \tag{5.10}$$
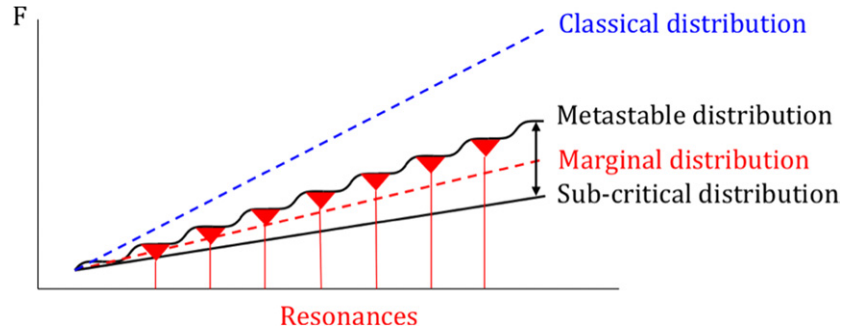
31

Figure 27. Diagram illustrating intermittent quasilinear relaxation due to resonance overlap in the multi-mode regime. The resonances broaden and eventually overlap as the modes grow above the instability threshold. The energetic-particle population drops to subcritical values and then is replenished by the source to a metastable level that exceeds the linear threshold level due to separation of neighbouring linear resonances.

This condition follows immediately from (5.2) and the estimate for the nonlinear bounce frequency obtained in [54],

$$\omega_{\mathrm{b}} \sim \gamma_0 \left(1 + \frac{\nu}{\gamma_{\mathrm{d}}} \right). \tag{5.11}$$

The significant difference between (5.9) and (5.10) for large values of N reflects the fact that the overlap of many resonances enhances the energy release per mode dramatically compared with the case of isolated modes. It is therefore possible that an overlap of two closely spaced resonances can trigger an avalanche-type relaxation event in which neighbouring modes become involved even if they are linearly stable.

Rapid quasilinear diffusion during such an event can reduce the energetic-particle population to a subcritical value that is below the linear instability threshold, as illustrated schematically in figure 27. The waves will then decay within the linear damping time, and the system will 'wait' until the particle sources restore the energetic-particle population to make it unstable and produce the next avalanche.

An intrinsic feature of such intermittent diffusion is that the bursts of different modes are synchronized because of the triggering effect. The bursts of many modes force the energetic-particle population to hover around the marginally stable level. This aspect is common to the steady and intermittent quasilinear regimes. The difference between the two is mainly in the time behaviour of the turbulence level. It is important to point out that the profile stiffness due to robust marginal stability condition actually means that the turbulence level adjusts itself to keep the same profile for stronger particle sources. The time averaged transport coefficients are then determined by the rate of injection and the gradients in the marginally stable profile whereas the specifics of turbulence that provides this enhanced transport is governed by small deviations from marginal stability. This situation makes it extremely difficult (but fortunately superfluous) to predict the level of turbulence in terms of few macroscopic parameters of the energetic-particle population (such as their pressure gradient or density gradient). Comparison between theory and experiment should then be focused not so much on the details of turbulence but rather on examining the marginal stability constrains and resonance overlap criteria, which requires adequate numerical tools to perform a comprehensive linear stability assessment for realistic magnetic configurations and plasma parameters.

The above mentioned trend for the level of turbulence to be less predictable than the modification of the fast-particle distribution pertains to numerical simulations of TAE bursts

and fast-ion losses in TFTR [107]. These simulations have reproduced such features as synchronization of multiple TAEs, the duty cycle of the bursts and the saturation of the stored beam energy. Yet, the mode saturation amplitude was significantly higher than that inferred from the experimental data. In an attempt to resolve this discrepancy, the numerical model has been generalized from the originally linearized description of the bulk plasma to the fully nonlinear MHD simulation of the bulk [18]. The description of energetic particles was nonlinear in both cases. Although the fully nonlinear simulations show some reduction in the mode saturation level, the calculated amplitudes are still several times greater than the estimated experimental values. The MHD nonlinearity introduces some interesting new elements into the problem, one of which is the generation of zonal flows that provide enhanced dissipation of Alfvénic modes. However, the saturated fast-particle population does not change in any significant way in the fully nonlinear case, which indicates robustness of the marginal stability regime.

The critical role of the resonance overlap condition for global transport has recently been confirmed in the analysis of fast-ion confinement in DIII-D. A significant flattening of NBI-produced energetic ions was observed in DIII-D experiments with reversed magnetic shear and numerous AC eigenmodes excited [108]. NBI into DIII-D plasmas with negative central shear produces a rich spectrum of AC modes and TAEs as NBI power increases above ∼1.4 MW. The fast-ion spectroscopy (FIDA) shows that the central fast-ion profile flattens in the discharge with Alfvénic activity, and neutron and equilibrium measurements corroborate the FIDA data. Figure 28(d) shows agreement between the experimentally measured neutron yield in the absence of Alfvénic activity and the yield predicted by the TRANSP code on the basis of the Coulomb collision transport mechanism. However, in the presence of Alfvénic activity, the experimentally measured neutron yield is lower than the expected one by ∼10–45%, as shown in figure 28(c).

Although the measured spectrum of modes reveals tens of different mode numbers, the effect of such modes on fast-ion transport is not always strong since many of these modes are localized in the vicinity of the same magnetic surface that has zero magnetic shear. Under such conditions, particularly careful measurements of the mode amplitudes and mode structure are needed in order to assess the possible role of the modes in energetic ion transport. In [108], such measurements were made and numerical modelling was performed for the beam ions' transport in the presence of multiple TAE and AC modes. However, the results of the initial modelling effort were mysterious: the calculations based on the measured mode amplitudes could not explain the observed significant transport of the fast ions. It was then realized that the initial simulations omitted the electric potential associated with the magnetic perturbations [17]. Only after proper care was taken about including both electric and magnetic perturbed fields in the analysis, did the wave–particle resonances meet the overlap condition. The resulting profiles of NBI-produced energetic ions computed with the ORBIT code were then found to be flattened in the presence of the modes, consistent with the measurements.

We conclude this section by discussing non-perturbative modes as a candidate for global transport of energetic particles. This mechanism involves mode frequency sweeping, which has attracted considerable attention in the energetic-particle studies. If the sweeping range is sufficiently broad, then the mode can reach the phase-space areas that are far away from the initial wave–particle resonance where the mode is excited. The effect of a single mode sweep is shown schematically in figure 29 for an idealized bump-on-tail model [110]. As a spontaneously created phase-space hole or clump propagates away from the original resonance, it modifies not just the oscillating part of the fast-particle distribution but the equilibrium distribution as well. The energy dissipation in the bulk plasma during the sweeping event makes this modification irreversible. As a result, in the absence of fast-particle collisions,
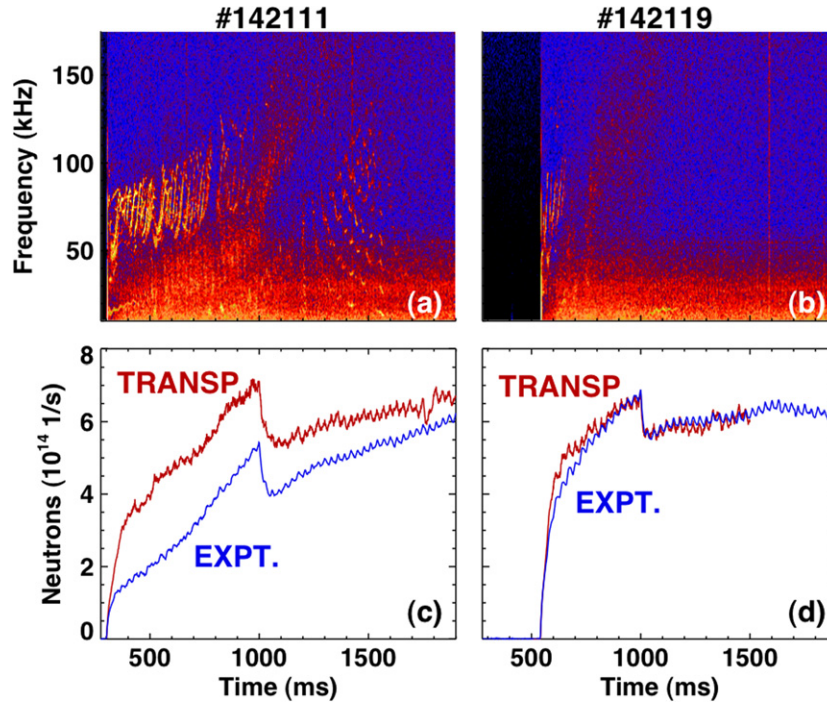
Figure 28. Spectra of interferometer signals and neutron emission data in two DIII-D discharges with and without significant Alfvénic activity (see [109]).
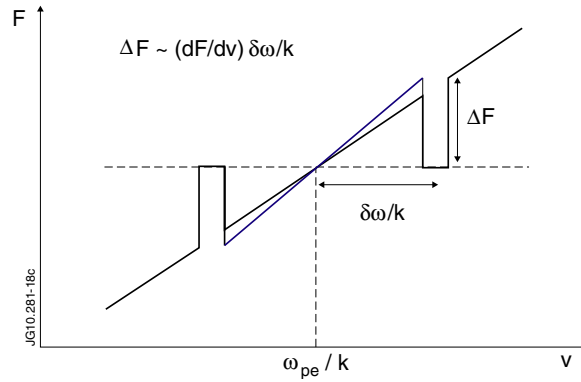

Figure 29. Diagram illustrating the motion of holes and clumps and the wake that acts to steepen to distribution function, creating a favourable environment for instability. Reprinted with permission from [110]. Copyright 2011, American Institute of Physics.

the equilibrium distribution will remain locally distorted when the sweep stops due to the lack of the energetic-particle drive far away from the original resonance. In the meantime, the original resonance generates new holes and clumps continuously. This can be understood by following the evolution of the 'wake' that forms when a hole or clump detaches from the original resonance. Referring to figure 29, since the particle number is conserved, a number of particles must be displaced during the motion of a hole or clump, which leads to a slight excess behind a hole and a depletion behind a clump. There is thus a tendency for the gradient
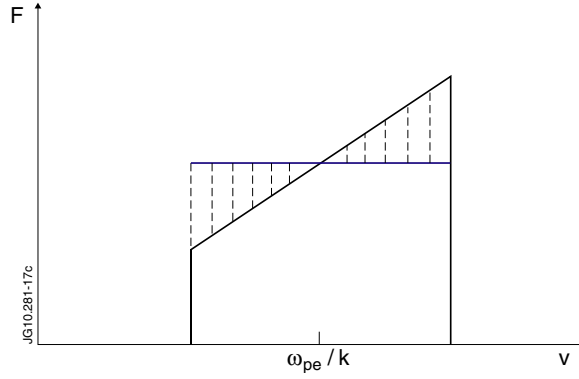
Figure 30. Diagram illustrating how holes and clumps might form a global plateaux in a distribution function with a finite extent in velocity space. The dashed lines mark the boundaries of the 'stacked up' holes and clumps. Reprinted with permission from [110]. Copyright 2011, American Institute of Physics.

in the distribution function to steepen, making the system susceptible to instability once again. This effect should be strongest when the hole and clump are still relatively close to the original resonance, which could explain why the holes and clumps are produced in rapid succession. The lack of drive away from the resonance due to the finite extent of the distribution in velocity-space limits the range of chirping for the initially formed holes and clumps. It is then reasonable to expect that eventually the holes and clumps will 'stack up' next to one another as they move away from the original resonance (see figure 30). In this way the distribution function should eventually form an extended plateaux that determines the maximum amount of energy that can be released from the fast particles to the wave. The waves should then decay due to dissipation, leaving a significantly deformed fast-particle distribution.

In the presence of fast-particle source and collisional relaxation processes, the multiple sweeping events can compete with classical collisions and reduce the fast-particle population considerably compared with the classical distribution, as observed in numerical simulations in [111]. To have significant macroscopic consequences, this mechanism requires energetic-particle collisions to be sufficiently low, so that the holes and clumps can affect a large part of the fast-particle distribution during their lifetime. The collisional lifetime of a hole or clump can be roughly estimated as [60, 110]

$$\tau \sim \nu_{\mathrm{diff}}^{-1}(\gamma_0/\omega)^2 \tag{5.12}$$

and the corresponding range of sweeping is

$$\frac{\delta\omega}{\omega} \sim \left(\frac{\gamma_0}{\omega}\right)^2 \sqrt{\frac{\gamma_0}{\nu_{\mathrm{diff}}}}, \tag{5.13}$$

where ν_{diff} is the energetic-particle collision frequency (for diffusive collisions) and γ_0 is the linear instability drive from the energetic particles.

It is interesting that the described strongly nonlinear relaxation process can reshape even stable initial distributions of the fast particles if there are finite amplitude perturbations that initiate the hole–clump production. The physics reason for that is that the formation of holes and clumps is an explosive process that represents a hard nonlinear regime. The role of the energetic-particle modes and multiple sweep relaxation scenario in real devices still needs to be assessed in comparison with the quasilinear scenario. This is one of the key unresolved issues in predicting the global transport of energetic particles.

6. More topics in progress

As already pointed out in the introduction, our selection of material for this review is inevitably subjective, which makes it appropriate to call attention to some of the interesting research topics that we have not covered here in any depth.

Alpha channelling. This is an exciting idea of using waves to transfer the alpha particle energy to the plasma ions to circumvent losses via the electron channel [112]. The waves can either be created by external rf sources or be self-generated due to alpha-particle-driven instabilities. In both cases, the challenge is to maintain a suitable spectrum of waves to provide resonant extraction of energy from a large fraction of the alpha particle population in phase space without anomalous spatial diffusion of the alpha particles. In the self-generated regime, one has also to find the means to control the nonlinear behaviour of the expected instabilities. One generally needs high-frequency instabilities (in the ion cyclotron frequency range) to utilize the energy of alphas with tolerable anomalous diffusion. However, in STs, one might also use the low-frequency modes with $n = 0$ to tap the free energy associated with poloidal bounces of the alpha particles near the trapped-passing boundary. The attempts to explore the idea of alpha channelling continue [113, 114], but the ongoing studies have not yet reached level of conclusive positive predictions with regard to fusion.

Background turbulence. Accurate transport analysis and measurements performed in recent years show that relaxation of fast ions may differ significantly from the classical predictions based on Coulomb collisions alone. In particular, this is observed as an 'anomaly' in the power deposition profile for NBI-produced energetic ions [115, 116]. On the other hand, it was found experimentally [21, 40] in reversed-shear discharges that a fairly slow beam can still excite numerous Alfvén modes with high toroidal mode numbers approaching those of thermal plasma turbulence. The effect of thermal plasma turbulence on fast ions has then attracted attention as a possible candidate for explaining the anomalous data [115, 116]. A detailed theoretical study has been performed in [117] to refine the orbit averaging argument for both electrostatic and magnetic perturbations. It was found that the electrostatic diffusivity of the beam ions decays as $1/E$ with the beam ion energy, while a similar magnetic quantity is independent of the beam energy. It remains to be seen yet whether a direct comparison between this theory and experiment is feasible.

TAEs and ripples. The enhancement of energetic-particle transport due to synergy between different types of perturbations is another important topic in view of burning plasma experiments. It was found experimentally on TFTR and explained theoretically in [118] that there is a violent loss mechanism due to the combined effect of magnetic ripples and TAEs excited by the energetic ions. This effect is called TAE-induced ripple trapping. It is caused by time-dependent TAE perturbations that increase the phase space of particles capable of entering the ripple-trapped area. As a result, the flux of energetic particles can be strong enough to damage the vacuum wall (as observed on TFTR [118]). Further investigation of such an effect is highly desirable in view of the ripples on ITER. However, experimental investigation of the TAE-ripple effect on existing machines, e.g. on JET, is hardly possible since this effect changes the poloidal distribution of the lost ions from the well protected mid-plane region to the less protected bottom of the machine.

Macroscopic equilibrium and stability. Significant advances in diagnostics of confined and lost energetic ions have made it possible to observe various types of interplays between energetic-particle-driven AEs and strong MHD perturbations such as sawteeth, ELMs and

NTMs (see, e.g., [119] and references therein). Moreover, some diagnostics designed for other purposes contribute a great deal to this effort. For example, the very fine time resolution achieved in neutron spectrometry has revealed the effects of MHD modes on the energy spectrum of DD neutrons [120]. In burning plasmas, the pressure of energetic particles can easily affect both, the equilibrium and MHD stability. The contribution of the fusion born alpha particles to the equilibrium current [121] was found to be essential in the ITER scenario with a low value of the inductive current, especially for the safety factor values close to integers (where transport and MHD stability are particularly sensitive to the current profile). Fast ions can potentially be used to stabilize the sawteeth. This possibility has recently been confirmed in cross-comparison experiments on JET, MAST, ASDEX-U and TEXTOR [122]. A combination of the fast-particle effects with the current drive affecting the magnetic shear at the $q = 1$ surface was found to be especially advantageous for the sawtooth control. Finally, it is conceivable, that the resistive wall modes [123], which are undesirable in high-β discharges, will be stable in the presence of fast particles, in a range of ITER-relevant parameters. Experimental investigation of this attractive idea is now pending.

Energetic ion physics in helical devices and stellarators. Along with the progress made in energetic-particle physics in tokamaks, the research of similar topics has also progressed significantly in helical devices and stellarators. The most remarkable achievements were reported from the LHD machine, in which hydrogen NBI of energy up to 180 keV drove strong AE activity at magnetic fields in the range from 0.4 to 3.0 T [124]. Analysis of the fast-ion confinement performed with NPA has shown a strong correlation between the fast change in energetic neutral fluxes and the AE bursts. Moreover, the observed changes in the NPA spectra seemingly indicated the formation of hole–clump pairs in the energetic-particle spectra associated with AE bursts in real space [125]. A direct comparison between the experimental observation and theory would be of considerable interest here.

Acknowledgments

References

[1] ITER Physics Basis 1999 *Nucl. Fusion* **39** 2137
[2] Cheng C Z, Chen L and Chance M S 1985 *Ann. Phys. (NY)* **161** 21
[3] Fu G Y and Van Dam J W 1989 *Phys. Fluids* B **1** 1949
[4] Wong K L *et al* 1991 *Phys. Rev. Lett.* **66** 1874
[5] Heidbrink W W *et al* 1991 *Nucl. Fusion* **31** 1635
[6] Wong K L 1999 *Plasma Phys. Control. Fusion* **41** R1
[7] Berk H L *et al* 2001 *Phys. Rev. Lett.* **87** 185002
[8] Sharapov S E *et al* 2001 *Phys. Lett.* A **289** 127
[9] Sharapov S E *et al* 2002 *Phys. Plasmas* **9** 2027
[10] Gryaznevich M P and Sharapov S E 2006 *Nucl. Fusion* **46** S942
[11] Fredrickson E D *et al* 2006 *Nucl. Fusion* **46** S926
[12] Sharapov S E *et al* 2004 *Phys. Rev. Lett.* **93** 165001
[13] Van Zeeland M A *et al* 2005 *Plasma Phys. Control. Fusion* **47** L31

[14] Snipes J A *et al* 2005 *Phys. Plasmas* **12** 056102
[15] Hacquin S *et al* 2007 *Plasma Phys. Control. Fusion* **49** 1371
[16] Kramer G J *et al* 2006 *Phys. Plasmas* **13** 056104
[17] White R B *et al* 2010 *Phys. Plasmas* **17** 056107
[18] Todo Y, Berk H L and Breizman B N 2010 *Nucl. Fusion* **50** 084016
[19] Goeldbloed J P *et al* 1993 *Plasma Phys. Control. Fusion* **35** B277
[20] Fasoli A *et al* 2002 *Plasma Phys. Control. Fusion* **44** B159
[21] Sharapov S E *et al* 2006 *Nucl. Fusion* **46** S868
[22] Berk H L, Breizman B N and Pekker M S 1996 *Phys. Rev. Lett.* **76** 1256
[23] Fasoli A *et al* 1998 *Phys. Rev. Lett.* **81** 5564
[24] Heeter R F *et al* 2000 *Phys. Rev. Lett.* **85** 3177
[25] Pinches S D *et al* 2004 *Plasma Phys. Control. Fusion* **46** S47
[26] Odblom A *et al* 2002 *Phys. Plasmas* **9** 155
[27] Candy J, Breizman B N, Van Dam J W and Ozeki T 1996 *Phys. Lett.* A **215** 299
[28] Kimura H *et al* 1998 *Nucl. Fusion* **38** 1303
[29] Shinohara K *et al* 2004 *Plasma Phys. Control. Fusion* **46** S31
[30] Nazikian R *et al* 2003 *Phys. Rev. Lett.* **91** 125003
[31] Sharapov S E, Mikhailovskii A B and Huysmans G T A 2004 *Phys. Plasmas* **11** 2286
[32] Breizman B N *et al* 2003 *Phys. Plasmas* **10** 3649
[33] Fu G Y and Berk H L 2006 *Phys. Plasmas* **13** 052502
[34] Breizman B N *et al* 2005 *Phys. Plasmas* **12** 112506
[35] Takechi M *et al* 2005 *Phys. Plasmas* **12** 082509
[36] Lauber Ph *et al* 2007 *Proc. 3rd IAEA TCM on Plasma Instabilities (York, UK, 26–28 March 2007)*
[37] Joffrin E *et al* 2003 *Nucl. Fusion* **43** 1167
[38] Austin M E *et al* 2006 *Phys. Plasmas* **13** 082502
[39] Beklemishev A D and Horton W 1992 *Phys. Fluids* B **4** 200
[40] Nazikian R *et al* 2006 *Phys. Rev. Lett.* **96** 105006
[41] Breizman B N 2006 *Theory of Fusion Plasmas: Joint Varenna–Lausanne Int. Workshop (Varenna, Italy)* ed O Sauter (New York: AIP) pp 15–26
[42] Abel I G, Breizman B N and Sharapov S E 2009 *Phys. Plasmas* **16** 102506
[43] Konovalov S V *et al* 2004 *Phys. Plasmas* **11** 4531
[44] Gorelenkov N N 2008 *Phys. Plasmas* **15** 110701
[45] Smith H *et al* 2006 *Phys. Plasmas* **13** 042504
[46] Edlund E 2009 *PhD Thesis* MIT
[47] Cheng C Z 1992 *Phys. Rep.* **211** 1
[48] Van Zeeland M A 2006 *Nucl. Fusion* **46** S880
[49] Edlund E M *et al* 2009 *Phys. Rev. Lett.* **102** 165003
[50] Van Zeeland M A *et al* 2006 *Phys. Rev. Lett.* **97** 135001
[51] Breizman B N, Berk H L, Pekker M S, Porcelli F, Stupakov G V and Wong K L 1997 *Phys. Plasmas* **4** 1559
[52] Berk H L, Breizman B N and Pekker M S 1997 *Plasma Phys. Rep.* **23** 778
[53] Bhatnagar P L, Gross E P and Krook M 1954 *Phys. Rev.* **94** 511
[54] Berk H L, Breizman B N and Ye H 1992 *Phys. Rev. Lett.* **68** 3563
[55] Lilley M K, Breizman B N and Sharapov S E 2009 *Phys. Rev. Lett.* **102** 195003
[56] Shinohara K *et al* 2001 *Nucl. Fusion* **41** 603
[57] Wong K L 1994 *Plasma Phys. Control. Fusion* **36** 879
[58] Saigusa M *et al* 1995 *Plasma Phys. Control. Fusion* **37** 295
[59] Bernabei S *et al* 2001 *Nucl. Fusion* **41** 513
[60] Berk H L, Breizman B N and Petviashvili N V 1997 *Phys. Lett.* A **234** 213
Petviashvili N 1999 *PhD Thesis* University of Texas at Austin
[61] Berk H L, Breizman B N, Candy J, Pekker M S and Petviashvili N V 1999 *Phys. Plasmas* **6** 3102
[62] Maslovsky D, Levitt B and Mauel M E 2003 *Phys. Plasmas* **10** 1549
[63] Fredrickson E D *et al* 2006 *Phys. Plasmas* **13** 056109
[64] Boswell C J *et al* 2006 *Phys. Lett.* A **358** 154
[65] Berk H L *et al* 2006 *Nucl. Fusion* **46** S888
[66] Winsor N, Johnson J L and Dawson J M 1968 *Phys. Fluids* **11** 2448
[67] Breizman B N 2010 *Nucl. Fusion* **50** 084014
[68] Bernstein I B, Greene J M and Kruskal M D 1957 *Phys. Rev.* **108** 546
[69] Chen L 1994 *Phys. Plasmas* **1** 1519

[70]   Zonca F, Briguglio S, Chen L, Fogaccia G and Vlad G 2005 *Nucl. Fusion* **45** 477
[71]   Chen L 2008 *Plasma Phys. Control. Fusion* **50** 124001
[72]   McGuire K *et al* 1983 *Phys. Rev. Lett.* **50** 891
[73]   Heidbrink W W *et al* 1990 *Nucl. Fusion* **30** 1015
[74]   Nave M F F *et al* 1989 *Proc. 16th EPS Conf. (Venice, Italy)* vol 13B P.2 p 05
[75]   Ninomya H *et al* 1988 *Proc. 12th Int. Conf. on Plasma Physics Controlled Fusion Research (Nice, France)* vol 1
          (Vienna: IAEA) pp 111
[76]   Gude A *et al* 1999 *Nucl. Fusion* **39** 127
[77]   Gryaznevich M P *et al* 2008 *Nucl. Fusion* **48** 084003
[78]   Arcis N and Sharapov S E 2008 *Phys. Lett.* A **372** 5807
[79]   Bussac M N *et al* 1975 *Phys. Rev. Lett.* **35** 1638
[80]   Chen L, White R B and Rosenbluth M N 1984 *Phys. Rev. Lett.* **52** 1122
[81]   Coppi B and Porcelli F 1986 *Phys. Rev. Lett.* **57** 2272
[82]   Coppi B, Migliuolo S and Porcelli F 1988 *Phys. Fluids* **31** 1630
[83]   Coppi B and Porcelli F 1988 *Fusion Technol.* **13** 447
[84]   Betti R and Freidberg J P 1993 *Phys. Rev. Lett.* **70** 3428
[85]   Porcelli F *et al* 1992 *Phys. Fluids* B **4** 3017
[86]   Gryaznevich M P *et al* 1998 *Phys. Rev. Lett.* **80** 3972
[87]   Kolesnichenko Y I *et al* 1999 *Phys. Rev. Lett.* **82** 3260
[88]   Kolesnichenko Y I *et al* 2001 *Proc. 28th EPS on Controlled Fusion and Plasma Physics (Funchal, Portugal,
          18–22 June 2001)* vol 25A (ECA) 1101
[89]   Kolesnichenko Y I *et al* 2006 *Phys. Plasmas* **13** 052504
[90]   Wong K L *et al* 2000 *Phys. Rev. Lett.* **85** 996
[91]   Zonca F *et al* 2007 *Nucl. Fusion* **47** 1588
[92]   Borba D *et al* 2000 *Nucl. Fusion* **40** 775
[93]   Putvinskii S V 1993 *Nucl. Fusion* **33** 133
[94]   Duong H H and Heidbrink W W 1993 *Nucl. Fusion* **33** 211
[95]   Nishiura M *et al* 2004 *Rev. Sci. Instrum.* **75** 3646
[96]   Perez von Thun C *et al* 2010 *Nucl. Fusion* **50** 084009
[97]   Joffrin E *et al* 2005 *Nucl. Fusion* **45** 626
[98]   Gill R D *et al* 1992 *Nucl. Fusion* **32** 723
[99]   Gruber O *et al* 1999 *Phys. Rev. Lett.* **83** 1787
[100] Heidbrink W W and Sadler G 1994 *Nucl. Fusion* **34** 535
[101] Sharapov S E and Hastie R J 1992 *Plasma Physics Notes* Culham Lab, 92/20
[102] Kadomtsev B B and Pogutse O P 1973 *Sov. Phys.—JETP* **39** 1012
[103] Strauss H R 1976 *Phys. Fluids* **19** 134
[104] Candy J, Berk H L, Breizman B N and Porcelli F 1999 *Phys. Plasmas* **6** 1822
[105] Fu G Y *et al* 2006 *Phys. Plasmas* **13** 052517
[106] Rosenbluth M N, Dagazian R Y and Rutherford P H 1973 *Phys. Fluids* **16** 1894
[107] Todo Y, Berk H L and Breizman B N 2003 *Phys. Plasmas* **10** 2888
[108] Heidbrink W W *et al* 2007 *Phys. Rev. Lett.* **99** 245002
[109] Van Zeeland M A *et al* 2011 *Phys. Plasmas* submitted
[110] Lilley M K, Breizman B N and Sharapov S E 2010 *Phys. Plasmas* **17** 092305
[111] Vann R G L, Berk H L and Soto Chavez A R 2007 *Phys. Rev. Lett.* **99** 025003
[112] Fisch N J and Rax J M 1992 *Phys. Rev. Lett.* **69** 612
[113] Fisch N J 2006 *Phys. Rev. Lett.* **97** 225001
[114] Fisch N J 2010 *J. Plasma Phys.* **76** 627
[115] Baranov Yu F *et al* 2009 *Plasma Phys. Control. Fusion* **51** 044004
[116] Heidbrink W W *et al* 2008 *Nucl. Fusion* **48** 084001
[117] Hauff T *et al* 2009 *Phys. Rev. Lett.* **102** 075004
[118] White R B *et al* 1995 *Nucl. Fusion* **35** 1707
[119] Kiptily V G *et al* 2009 *Nucl. Fusion* **49** 065030
[120] Hellesen C *et al* 2010 *Nucl. Fusion* **50** 022001
[121] Yavorskij V *et al* 2009 *Proc. 11th IAEA TCM on Energetic Particles (Kiev, Ukraine, 23–25 September 2009)*
[122] Chapman I T *et al* 2008 *Proc. 22nd IAEA Fusion Energy Conf. (Geneva, Switzerland, 13–18 October 2008)*
[123] Bo Hu, Betti R and Manickam J 2005 *Phys. Plasmas* **12** 057301
[124] Toi K *et al* 2000 *Nucl. Fusion* **40** 1349
[125] Osakabe M *et al* 2006 *Nucl. Fusion* **46** S911